

# Interferometric Single-Shot Parity Measurement in an InAs-Al Hybrid Device

Microsoft Azure Quantum<sup>†</sup>  
(Dated: February 15, 2024)

The fusion of non-Abelian anyons or topological defects is a fundamental operation in measurement-only topological quantum computation. In topological superconductors, this operation amounts to a determination of the shared fermion parity of Majorana zero modes. As a step towards this, we implement a single-shot interferometric measurement of fermion parity in an indium arsenide-aluminum heterostructure with a gate-defined nanowire. The interferometer is formed by tunnel-coupling the proximitized nanowire to quantum dots. The nanowire causes a state-dependent shift of these quantum dots' quantum capacitance of up to 1 fF. Our quantum capacitance measurements show flux  $h/2e$ -periodic bimodality with a signal-to-noise ratio of 1 in 3.7  $\mu$ s at optimal flux values. From the time traces of the quantum capacitance measurements, we extract a dwell time in the two associated states that is longer than 1 ms at in-plane magnetic fields of approximately 2 T. These results are consistent with a measurement of the fermion parity encoded in a pair of Majorana zero modes that are separated by approximately 3  $\mu$ m and subjected to a low rate of poisoning by non-equilibrium quasiparticles. The large capacitance shift and long poisoning time enable a measurement error probability of 1%.

## 1. INTRODUCTION

In order to leverage a topological phase for quantum computation, it is crucial to manipulate and measure the topological charge. This can be achieved through protected operations such as braiding and fusing non-Abelian anyons, which offer exponential suppression of errors induced by local noise sources and a native set of discrete operations [1–3]. Protocols for measurement-only topological quantum computation simplify these operations, reducing them to fusion alone [4–6]. This fundamental measurement is sufficient to enact all topologically protected operations. Novel error correction schemes have been developed to take advantage of the operations available in measurement-only topological quantum computation [7–10]. The robustness against errors and simplicity of control offered by this approach make measurement-based topological qubits a promising path towards utility-scale quantum computation, where managing the interactions of millions of qubits is necessary [11–14].

One-dimensional topological superconductors (1DTSs) [15–17] are a promising platform for building topological qubits [18]. Quantum information is stored in the fermion parity of Majorana zero modes (MZMs) localized at the ends of superconducting wires [19–21], and projective measurements of the fermion parity are used to process quantum information and perform qubit state readout [22–24]. The fermion parity shared by a pair of MZMs can be determined through an interferometric measurement [16, 25–34]. A number of conceptual designs for topological qubits incorporate such interferometers [6, 35–40]. Progress in this direction was made in Ref. 41, which reported coherent transport through a gate-defined nanowire island in an Aharonov–Bohm interferometer, albeit in a regime that does not allow qubit readout.

In this paper, we demonstrate an interferometric measurement of the parity of a low-energy state in a 1D

nanowire, thereby validating a necessary ingredient of topological quantum computation. The measurement technique is based on probing the quantum capacitance  $C_Q$  of a quantum dot coupled to the nanowire and allows determination of the parity in a single shot, with a minimum probability of assignment errors of 1%. By itself, this measurement does not distinguish between MZMs in the topological phase and fine-tuned low-energy Andreev bound states in the trivial phase [42–45], but it does require the low-energy state to be supported at both ends of the wire, and provides a measurement of its energy with single- $\mu$ eV resolution. These features of the measurement strongly constrain the nature of the low-energy state. In a follow-up paper [46], we will discuss parity measurements in the topological phase identified by the topological gap protocol (TGP) [47, 48].

## 2. TOPOLOGICAL QUBIT DEVICE DESIGN AND SETUP

In this work, we introduce a topological qubit design that allows one to perform projective measurements of fermion parity encoded in MZMs. The device is composed of two primary components, as illustrated in Fig. 1. The first component is a nanowire, sections of which can be tuned into a 1DTS state, leading to topological degeneracy of the many-body ground state. The second component consists of quantum dots, which are designed to couple pairs of MZMs in an interferometric loop. This device's 1DTS is based on a gated superconductor-semiconductor heterostructure [48–51]. The active region of the semiconductor consists of a 9.1 nm thick InAs quantum well with a 6 nm thick  $\text{In}_{0.88}\text{Al}_{0.12}\text{As}$  top barrier and 25 nm thick  $\text{In}_{0.845}\text{Al}_{0.155}\text{As}$  lower barrier, depicted schematically in Fig. 1a. The superconductor is a 60 nm wide Al strip (blue in Fig. 1) deposited with a thickness of 6.5 nm on the semiconductor. The material combination and dimensions have been optimized for values

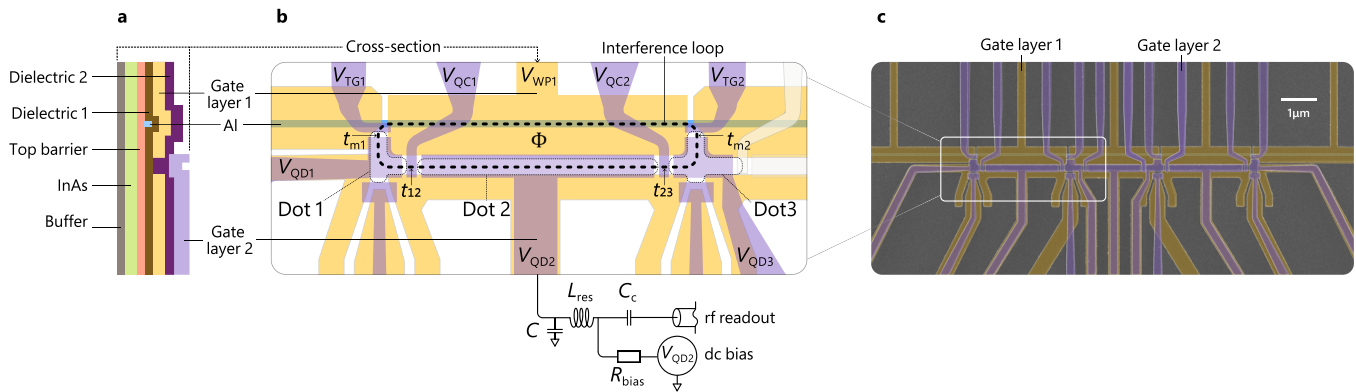


FIG. 1. (a) Cross-section of the topological qubit device design. (b) Simplified schematic picture of the gate layout for the interference loop formed by the triple-quantum-dot and the gate-defined nanowire. See Fig. 6 and Appendix A 1 for a complete device schematic and gate naming convention; throughout the paper  $V_x$  refers to the voltage applied to gate  $x$ . The interferometer loop used for readout is indicated with a dashed line. QD2 is routed to an off-chip resonator chip for dispersive gate sensing and  $C_Q$  measurement, and which also includes a bias tee circuit for applying dc bias. More details on the electronic setup can be found in the schematic in Fig. 7 of the Appendix. (c) An SEM image with the aluminum strip (blue), first gate layer (yellow), and second gate layer (purple) indicated in false color.

of the induced gap, spin-orbit coupling, and localization length that are favorable for the topological phase. Device fabrication and the details of the heterostructure design are discussed in Appendix A 2 and Appendix A 3, respectively.

In the full device, the nanowire is divided into 5 segments; one of them is shown schematically in Fig. 1b while all 5 are visible in Fig. 1c. Each has a different “plunger” gate in the first gate layer (yellow in Fig. 1) that controls the density in the corresponding region of the InAs quantum well. To form a qubit, the second and fourth segments, each of length  $L \approx 3 \mu\text{m}$  long, need to be tuned into the topological phase while the other three need to be fully depleted underneath the Al nanowire (see Fig. 6 in Appendix A for details). In this configuration, these trivial regions separate the two topological sections from each other and from Ohmic contacts at the ends of the Al nanowire [52]. A full qubit device therefore consists of two 1DTS, each containing a pair of MZMs, separated by a trivial section in the middle, and three interferometers that are used to couple neighboring pairs of MZMs. The complete gate layout, abbreviations for the different gates, and the voltage configuration for operation as a qubit are described in Appendix A. Here, we focus on the left topological section of the device, shown in Fig. 1b, and implement a parity measurement using its associated interferometer.

Our readout circuit is based on dispersive gate sensing of a triple quantum dot interferometer (TQDI): three electrostatically defined quantum dots that together with the 1DTS form a loop (Fig. 1b) threaded by a flux,  $\Phi$ . We control  $\Phi$  by varying the out-of-plane magnetic field,  $B_{\perp}$ . The TQDI has two smaller dots (dots 1 and 3) connected to the ends of the 1DTS through tunnel couplings  $t_{mi}$ , where  $i = 1, 2$ , and a long quantum dot (dot 2) that connects to dot 1 (dot 3) through tunnel couplings  $t_{12}$  ( $t_{23}$ ). The quantum capacitance,  $C_Q$ , of dot 2

is read out through dispersive gate sensing using an off-chip resonator circuit in a reflectometry setup [53–61]. To improve the signal-to-noise ratio (SNR), a Josephson Traveling Wave Parametric Amplifier (JTWPA) [62] is used in the first stage of amplification, followed by a low-noise high-electron-mobility transistor (HEMT) amplifier. Filtering is applied to dc lines as well as the rf readout lines to reduce the noise and radiation incident from higher temperature stages. Isolation on the rf lines is used to further reduce in-band back-action from the reflectometry setup. In addition to the line filtering and isolation, we employ multiple layers of shielding of the sample to suppress the generation of non-equilibrium quasiparticles (QPs) by stray infrared radiation [63, 64]. A detailed description of the reflectometry setup is given in Appendix A 4.

Our TQDI device design addresses two crucial challenges. First, the device size is subject to conflicting requirements. To suppress the Majorana splitting  $E_M \sim \Delta_T \exp(-L/\xi)$ , we require  $L \gg \xi$  (where  $\xi$  is the disordered coherence length and  $\Delta_T$  is the topological gap). However, an increase in  $L$  also suppresses (albeit algebraically) the level spacing and charging energy of the dot, which suppresses the interference signal, as we discuss in Appendices B 3 and D. Our triple dot design offers a solution to these issues. With a length of  $2.4 \mu\text{m}$ , dot 2 retains a charging energy of  $\approx 60 \mu\text{eV}$  deep in the Coulomb blockade regime, which is renormalized down to  $\approx 45 \mu\text{eV}$  in the interferometer’s operating regime. The level spacing is  $\approx 20 \mu\text{eV}$  (see also Appendix C 2). To minimize the effect of disorder within dot 2, which may hinder elastic co-tunneling, we operate the dot with an occupation of  $\sim 1000$  electrons. Dot 2 has significant effective tunneling matrix elements to both ends of the wire via the small dots of effective length  $400\text{--}500 \text{ nm}$ . The effective dot-to-wire couplings,  $t_L$  and  $t_R$ , can be fine-tuned by adjusting the microscopic parameters that determine

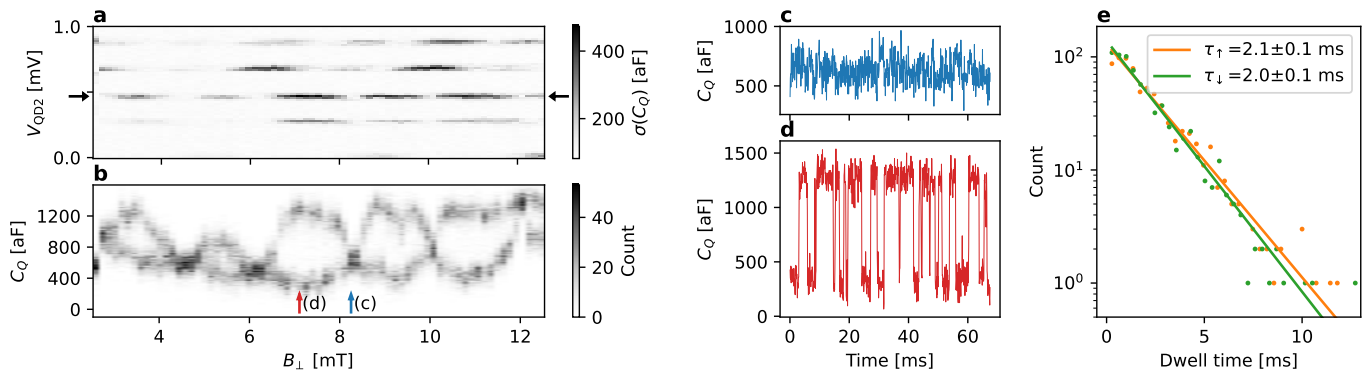


FIG. 2. (a) The standard deviation in the quantum capacitance  $\sigma(C_Q)$  as a function of  $B_{\perp}$  (which controls  $\Phi$ ) and  $V_{QD2}$  (which controls the dot 2 detuning) in the  $B_{\parallel}, V_{WP1}$  parameter regime where we expect the topological phase. (b) A histogram of  $C_Q$  values as a function of flux for the  $V_{QD2}$  value indicated by the black arrows in panel (a), showing clear bimodality that is flux-dependent with period  $h/2e$ . (c-d) Time traces at the two flux values marked by the vertical arrows in panel (b), corresponding to minimal (blue) and maximal (red)  $\Delta C_Q$ . (e) A histogram of dwell times aggregated over all values of  $B_{\perp}$  where the signal shows bimodality. Fitting to an exponential shows that the up and down dwell times are 2.0(1) ms and 2.1(1) ms and agree to within the standard error on the fits.

them:  $t_{12}, t_{23}, t_{m1}, t_{m2}, N_{g1}, N_{g3}$ . The tunnel couplings,  $t_{ij}, t_{mi}$  are indicated in Fig. 1b. The dimensionless gate offset charge  $N_{gi}$  is controlled by the gate voltage  $V_{QDi}$  and is given (up to an offset) by  $N_{gi} = \alpha_i e V_{QDi} / (2E_C)$  where  $\alpha_i$  is the lever arm of the associated gate, and  $E_C$  is the charging energy of the dot. The relationship between the microscopic parameters and an effective model is further described in Appendix B 2.

The second challenge that this design addresses is the need for a substantial lever arm for QD2, which is the gate that couples the dot to the readout resonator. The signal amplitude is determined by the quantum capacitance,  $C_Q^{(n)} = -e^2 \alpha^2 \partial^2 \varepsilon_n / \partial E_D^2$ , for a state  $n$  in TQDI configuration with energy  $\varepsilon_n$  with  $E_D$  being the detuning of dot 2 from the charge degeneracy point. We have optimized the lever arm by using a dual-layer gate geometry which enables us to place the plunger directly over the dot. As detailed in Appendix B, both simulations and measurements confirm that QD2 has a lever arm  $\alpha \approx 0.4 - 0.5$ . Combined with our high bandwidth dispersive gate sensing setup and low-noise parametric amplifier that operates close to the quantum limit, this lever arm ensures that we can detect  $C_Q$  with sufficient SNR. Readout can be activated by tuning all dots into resonance with the MZMs and by setting the effective tunnel couplings between dot 2 and the MZMs,  $t_L$  and  $t_R$ , sufficiently high and balanced.

Our device permits both dc and rf measurements, enabling the development of an rf-based QD-MZM tuning protocol that we use to balance the arms of the interferometer. The protocol uses a measurement of  $C_Q$  in a configuration where one of the small dots is maximally detuned to effectively interrupt the loop. These measured quantities are fit to simulations to extract the couplings  $t_{12}, t_{23}, t_{m1}$ , and  $t_{m2}$  (see Appendix D). This measurement protocol expands upon the technique proposed in Refs. 65 and 66 and demonstrated in Ref. 67

which was based on dc transport measurements of the coupling between a quantum dot and a zero-energy state in a nanowire. However, our rf-based protocol offers a finer resolution for the extraction of the couplings (down to single- $\mu$ eV level) and, thus, enables tuning the effective dot-to-wire couplings  $t_L$  and  $t_R$ . Once we have determined the appropriate voltages for QD1 and QD3, we proceed with interferometer measurements. We can move through the bulk phase diagram of the nanowire by varying the in-plane field  $B_{\parallel}$  and the voltage  $V_{WP1}$ , indicated in Fig. 1b. Appendix C contains further details of the tuneup procedure which leads to the neighborhood of  $B_{\parallel} = 1.8$  T and  $V_{WP1} = -1.832$  mV. Complete details of tuning the nanowire into the topological phase will be discussed in [46].

### 3. FERMION PARITY MEASUREMENT AND INTERPRETATION

To measure a time record of the fermion parity, we tune up the TQDI and perform a sequence of close to  $1.5 \times 10^4$  consecutive measurements of the resonator response, each with an integration time of 4.5  $\mu$ s, thereby recording a time trace of total length 67 ms. To improve visibility and make connection with theoretical predictions, we downsample the time trace to a resolution of 90  $\mu$ s and convert the resonator response into a  $C_Q$  record using the procedure discussed in Appendix A 5. We also sweep  $V_{QD2}$  and the out-of-plane magnetic field  $B_{\perp}$  in steps of 0.14 mT to study the dependence on the external flux  $\Phi$  through the interferometer loop.

When the wire is tuned into the topological regime and dot 2 is tuned to charge degeneracy, we observe oscillations in the standard deviation  $\sigma(C_Q)$  of the  $C_Q$  time trace with a period of 1.7(2) mT (Fig. 2a). This period is close to the 1.7 mT expected to produce a flux of  $h/2e$

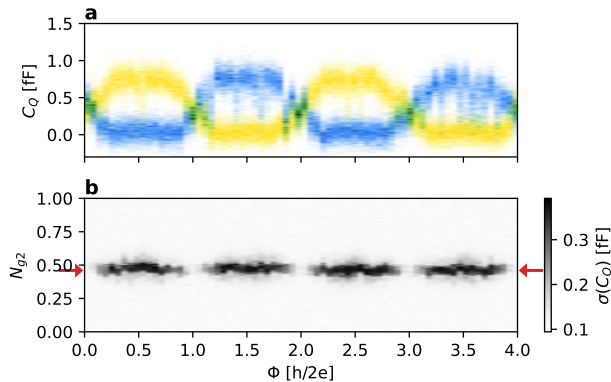


FIG. 3. Simulated dynamical  $C_Q$  as a function of magnetic flux and dot 2 gate offset charge  $N_{g2}$ , including the effects of charge and readout noise, as well as non-zero temperature, drive power, and frequency, per the discussion in the text. (a) Histogram of the two parity sectors for fixed  $N_{g2} = 0.49$ . Here, we used  $t_{m1} = t_{m2} = 6 \mu\text{eV}$ ,  $t_{12} = t_{23} = 8 \mu\text{eV}$ ,  $E_{C1} = 140 \mu\text{eV}$ ,  $E_{C2} = 45 \mu\text{eV}$ ,  $E_{C3} = 100 \mu\text{eV}$ ,  $N_{g1} = N_{g3} = 0.3$ ,  $T = 75 \text{mK}$ , and  $E_M = 0$ . (b) Standard deviation of  $C_Q(t)$  as a function of  $N_{g2}$  and flux through the loop. The red arrows indicate the  $N_{g2}$  value used for the linecut in (a).

through the interference loop in this device geometry. The visibility and phase of the oscillations varies between successive charge transitions in dot 2. This observed behavior is consistent with what one would anticipate for a disordered quantum dot, the properties of which are described by random matrix theory [68]. Indeed, a similar difference in visibility of flux-induced oscillations across different charge transitions was recently observed in a double quantum dot interferometer experiment [69]. In Sec. 4, we discuss oscillations with different periods that are observed at other points in the device's parameter space.

Histograms of the  $C_Q$  time trace for one of the dot 2 transitions reveal that its large standard deviation  $\sigma(C_Q)$  originates from a bimodal distribution of  $C_Q$  values, as shown in Fig. 2b. The time evolution of  $C_Q$  exhibits a random telegraph signal (RTS) at flux values where there is clear bimodality, as in Fig. 2d, but no telegraph signal in the absence of bimodality, as in Fig. 2c. As demonstrated in Fig. 2e, the intervals between switches follow an exponential distribution with a characteristic time of  $\tau_{\text{RTS}} \approx 2 \text{ms}$ . From the histograms, we extract an achieved SNR of 1 in  $3.7 \mu\text{s}$ , see Fig. 9. We interpret these  $h/2e$ -periodic bimodal oscillations and RTS in  $C_Q$  as originating from switches of fermion parity. Such switches have been observed in mesoscopic superconducting devices, where they were triggered by non-equilibrium QPs that infiltrated from the superconducting leads [42, 43, 45, 63, 70–80].

We support this interpretation by reproducing our results with quantum dynamics simulations that incorporate rf drive power, charge noise, and temperature. To

build intuition for those simulations, we use an idealized model (see Appendix B) subject to the follow assumptions: the wire is in the topological phase and there are no sub-gap states other than the MZMs; the charging energy and level spacing in the dots are much greater than the temperature; dot 1 and dot 3 are sufficiently detuned that their influence is fully encapsulated in the effective couplings  $t_L$  and  $t_R$  to MZMs at the ends of the wire; the drive frequency and power are both negligible; and there are no low-energy states in the wire except for those corresponding to the fermion parity. In this limit, the quantum capacitance as a function of the total fermion parity in the QD-wire system,  $Z$ , is given by:

$$C_Q(Z, \phi) = \frac{2e^2\alpha^2|t_C(Z, \phi)|^2}{[(E_D + 2ZE_M)^2 + 4|t_C(Z, \phi)|^2]^{3/2}} \times \tanh\left(\frac{\sqrt{(E_D + 2ZE_M)^2 + 4|t_C(Z, \phi)|^2}}{2k_B T}\right), \quad (1)$$

where  $E_D$  is the detuning from the charge degeneracy point,  $\alpha$  is the lever arm of the plunger gate to the dot,  $E_M$  is the MZM energy splitting, and  $T$  is the temperature. The net effective tunneling that results from the interference between different trajectories from the dot to the MZMs and back,  $t_C(Z, \phi)$ , is

$$|t_C(Z, \phi)|^2 = |t_L|^2 + |t_R|^2 + 2Z|t_L||t_R|\sin\phi. \quad (2)$$

Here,  $\phi$  is the phase difference between  $t_L$  and  $t_R$ , which is controlled by the magnetic flux  $\Phi$  through the interference loop created by the dot, the wire, and the tunneling paths between them according to  $\phi = 2\pi\Phi/\Phi_0 + \phi_0$ , where  $\Phi_0 = h/e$  and  $\phi_0$  is a flux-independent offset. To capture the extent to which  $C_Q$  can be used to discriminate between  $Z = \pm 1$ , it is convenient to introduce

$$\Delta C_Q(\phi) = |C_Q(1, \phi) - C_Q(-1, \phi)|. \quad (3)$$

The interferometer must be well-balanced  $t_L \sim t_R$  in order for  $\Delta C_Q$  to be large. When  $E_M = 0$ ,  $\Delta C_Q$  exhibits maxima along the  $E_D = 0$  line, with flux periodicity  $h/2e$ . In the presence of finite splitting  $E_M \neq 0$ , the  $Z = 1$  maxima form an  $h/e$ -periodic arrangement along the  $E_D = -2E_M$  line while the  $Z = -1$  maxima form a similar arrangement along the  $E_D = 2E_M$  line, but out of phase by a flux offset of  $h/2e$ .

For detailed comparison with experiments, we simulate a more complete model of our interferometer, expanded to include the full triple-dot system, incoherent coupling to the environment, and backaction from the measurement. As before, we neglect all states in the wire except the MZMs. Using the methods discussed in Appendices B 4 and D, we compute  $C_Q$  at temperature  $T = 75 \text{mK}$ ; charge-noise-induced dephasing rate  $\gamma = 1 \text{GHz}$ ; drive frequency  $\omega = 2\pi \times 500 \text{MHz}$ ; and detuning drive amplitude  $A_{\text{rf}} = 5 \mu\text{eV}$ . These values for the temperature and charge noise are based on quantum dot measurements in our system, which we discuss in more detail elsewhere [46].

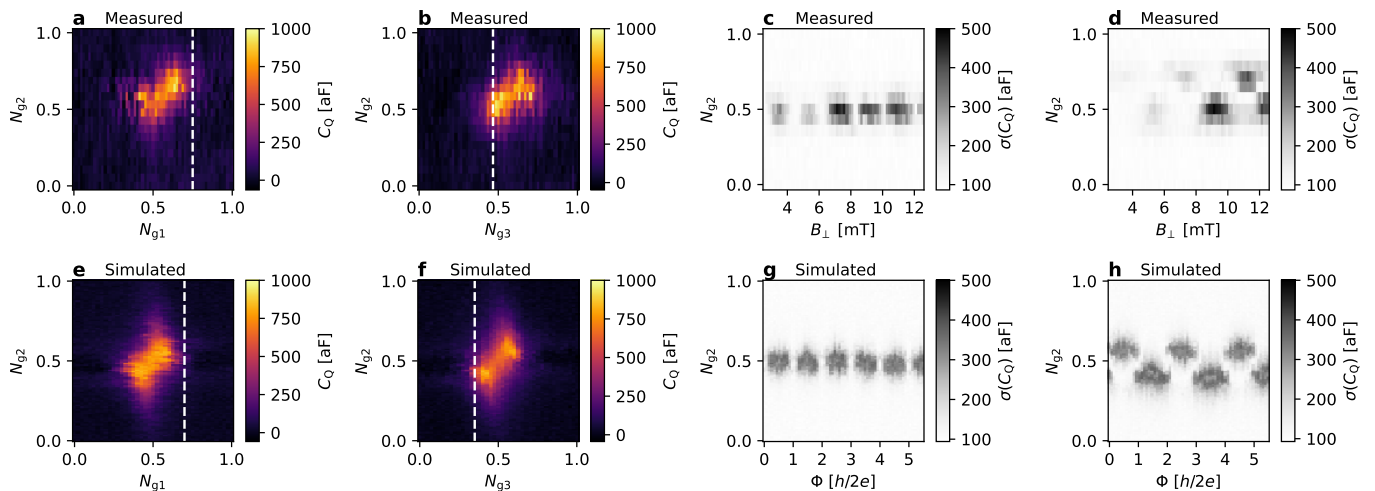


FIG. 4. (a-b) The measured gate-gate scans used to extract the QD-MZM couplings and (c) the standard deviation of the resonator response in TQDI configuration, taken at the same point in the  $(B_{\parallel}, V_{\text{WP1}})$  phase diagram. The dashed lines indicate the points in  $N_{g1}$  and  $N_{g3}$  where the data in panels (c) and (d) were taken. (d) The standard deviation in the resonator response with  $V_{\text{WP1}}$  increased by 0.39 mV relative to (c). Note that the bimodality is not visible at small  $B_{\perp}$  here due to the movement of the resonator frequency with field. (e-f) Simulated gate-gate scans which are fit to the experimental data in panels (a) and (b) in order to extract the QD-MZM couplings. (g) The simulated standard deviation in the resonator response for the same couplings and with  $E_M = 0$ . (h) The simulated standard deviation in the resonator response in the topological phase with only  $E_M$  modified to  $E_M = 3 \mu\text{eV}$ .

The simulated dynamical  $C_Q$  is shown in Fig. 3. The  $C_Q$  histograms in Fig. 3a reveal two  $h/e$ -periodic branches (one shown in yellow and the other in blue), associated with the two parities of the coupled system. For  $t_{m1} = t_{m2} = 6 \mu\text{eV}$ ,  $t_{12} = t_{23} = 8 \mu\text{eV}$ ,  $E_{C1} = 140 \mu\text{eV}$ ,  $E_{C2} = 45 \mu\text{eV}$ ,  $E_{C3} = 100 \mu\text{eV}$ ,  $N_{g1} = N_{g3} = 0.3$ , our simulations yield an estimated maximum value as a function of flux  $\Delta C_Q \approx 1 \text{ fF}$ , which is close to the measured value shown in Fig. 2d.

If the fermion parity  $Z$  were perfectly conserved, then the device would remain in one of the two parity eigenstates and the  $\Phi$  dependence would follow either the blue or the yellow trace in Fig. 3a. However,  $Z$  fluctuates on a time scale given by the quasiparticle poisoning time  $\tau_{\text{qpp}}$ . Hence, in traces over times longer than  $\tau_{\text{qpp}}$ , a bimodal distribution of  $C_Q$  values is expected, i.e. *both* the blue and yellow traces in Fig. 3a. Consequently, the standard deviation  $\sigma(C_Q)$  is peaked where  $\Delta C_Q$  is peaked, as shown in Fig. 3b, and time traces taken at these points will exhibit a telegraph signal composed of switches between the values  $C_Q(1, \phi)$  and  $C_Q(-1, \phi)$ .

Experimentally, we can perform additional checks to verify RTS in Fig. 2d can be attributed to switches of the fermion parity caused by quasiparticle poisoning events. As a first check, we can estimate the non-equilibrium quasiparticle density  $n_{\text{qp}}$  from the rate at which the combined QD-MZM system absorbs a non-equilibrium quasiparticle, setting  $\tau_{\text{qpp}} \equiv \tau_{\text{RTS}}$ , and verify consistency with an independent, more direct, measurement. The rate of such absorption of a non-equilibrium quasiparticle can be estimated via  $\tau_{\text{qpp}}^{-1} = \gamma_0 \zeta n_{\text{qp}} \mathcal{V}$ , where  $1/\gamma_0 \sim 1 \text{ ns}$  is a typical time scale for a quasiparticle to relax via electron-

phonon coupling [81] and become trapped in the topological wire segment,  $\zeta$  is the probability that an above-parent-gap quasiparticle is in the InAs forming the topological segment,  $\mathcal{V}$  is the volume of the superconductor in contact with the topological segment, and  $n_{\text{qp}}$  is the density of quasiparticles in Al. The weight  $\zeta$  is suppressed by the ratio of the semiconductor to superconductor densities of states and is typically of the order of  $\zeta \sim 10^{-3}$  in the single subband regime [48, 82]. Within this model, poisoning time scales of  $\tau_{\text{qpp}} \sim 2 \text{ ms}$  arise from a non-equilibrium quasiparticle density  $n_{\text{qp}} \sim 1 \mu\text{m}^{-3}$ .

In a separate experiment detailed in Appendix E, we study the quasiparticle poisoning phenomenon using a Cooper pair box device which is filtered and shielded from radiation in a manner similar to the device in Fig. 1 (see Appendix A 4). Using DGS, we measure the quantum capacitance of a Cooper pair box [74, 75] and observe even-odd switching events in real time. This enables us to extract the density of non-equilibrium quasi-particles in the Al strip, yielding  $n_{\text{qp}}^{\text{CPB}} = 0.6 \mu\text{m}^{-3}$ . This is comparable to the density estimated from  $\tau_{\text{RTS}}$  and is similar to the densities measured in prior studies [42, 43, 45, 63, 70–73, 76–80].

As a second check, we can exclude the possibility that the RTS arises from two-level systems in the vicinity of the device, an effect which has been commonly observed in quantum dots and quantum point contacts [83–86]. A control experiment can check for this possibility by suppressing  $t_{m1}, t_{m2}$ , thereby reducing tunneling between the wire and the triple-dot, which should increase  $\tau_{\text{RTS}}^{-1}$ . As a third check, we can intentionally introduce quasiparticles in the device and check that  $\tau_{\text{RTS}}^{-1}$  increases as

a result. The latter two checks will be presented in a separate publication [46].

#### 4. DIFFERENT OBSERVED INTERFEROMETRY REGIMES

The oscillations shown in Fig. 2b are the easiest to interpret but they are not the only type of oscillations that we observe when we vary the voltage  $V_{\text{WP1}}$  by 1 – 2 mV in the ostensible topological regime. In this section, we show how they can be explained within the model discussed in the previous section (see Appendix B for more details of the model).

To apply this model, we first extract the model parameters  $t_{m1}$ ,  $t_{m2}$ ,  $t_{12}$ , and  $t_{23}$  (along with the charges  $N_{gi}$  and charging energies). In order to do this, we fit the measured response consistently in three different configurations: (i) Dot 3 is maximally detuned, (ii) Dot 1 is maximally detuned, and (iii) all dots are optimally tuned to balance the interferometer. The couplings  $t_{m1}$ ,  $t_{m2}$ , and  $t_{12} \sim t_{23}$  are set by the procedure summarized at the end of Sec. 2. As an example, the scan shown in Fig. 4a can be quantitatively compared to the simulated data in Fig. 4e to determine the couplings  $t_{12}$  and  $t_{m1}$ . This scan is taken with dot 3 detuned, which cuts off the right arm of the interferometer. The extent of the bright region in the  $N_{g1}$  direction in Fig. 4a is correlated with  $t_{m1}$  while the extent along the  $N_{g1} - N_{g2}$  diagonal is correlated with  $t_{12}$  (see Appendix D for details). Similarly, Fig. 4b and Fig. 4f (taken with the left arm of the interferometer cut) are used to determine the couplings  $t_{23}$  and  $t_{m2}$ . This leaves us with one independent parameter  $E_M$ , which can be fitted to  $\sigma(C_Q)$  data when both arms of the interferometer are connected.

We now classify the various types of oscillations that we have observed according to the following scenarios:

- (a) The standard deviation  $\sigma(C_Q)$  is flux-dependent with a period of  $h/2e$ , as illustrated in Fig. 4c. The histogram of  $C_Q$  values shows bimodality with this period, as shown in Fig. 2b and Fig. 5a. We interpret this scenario as resulting from a balanced interferometer with two parity branches, both of which exhibit clear  $h/e$  periodicity.
- (b) The standard deviation  $\sigma(C_Q)$  exhibits a characteristic  $h/e$ -periodic zig-zag pattern, as shown in Fig. 4d. A fixed- $V_{\text{QD2}}$  horizontal cut through the  $\sigma(C_Q)$  plot has  $h/e$ -periodicity, and the histogram of  $C_Q$  values shows bimodality with  $h/e$ -periodic oscillations that are more pronounced in one branch, as in Fig. 5b. We identify this scenario with a balanced interferometer with two parity branches, one of which has stronger flux dependence than the other at a fixed value of  $N_{g2}$ .
- (c) There is bimodality, but neither  $\sigma(C_Q)$  nor the histogram of  $C_Q$  values shows visible periodicity in

flux, as shown in Fig. 5c. This scenario can be interpreted as a very unbalanced interferometer, resulting in an absence of distinct flux dependence in either of parity branches.

We begin by explaining scenario (a) in terms of a balanced interferometer model with a small  $E_M$  value. Applying the procedure described above to the dataset discussed in Fig. 4a-c, we obtain the following model parameters for the particular charge transition point in that figure:  $t_{m1} \approx 6 \mu\text{eV}$ ,  $t_{m2} \approx 4 \mu\text{eV}$ ,  $t_{12} \approx t_{23} \approx 12 \mu\text{eV}$ , and  $E_M \approx 0$ . These parameters lead us to Fig. 4e-g and Fig. 5d. A close examination reveals good agreement between the measured (Fig. 5a) and simulated (Fig. 5d) data. Hence, scenario (a) can be explained by  $t_{m2} \sim t_{m1}$  and small  $E_M$ .

In order to delve into scenario (b), we analyze the dataset displayed in Fig. 5b (corresponding to a cut at  $N_{g2} = 0.5$  in Fig. 4d) and Fig. 5e. Oscillations with period  $h/e$  are apparent in one of the parity branches in Fig. 5b<sup>1</sup> and e, thereby realizing scenario (b). This dataset is offset by  $\Delta V_{\text{WP1}} = 0.39$  mV from the data in Fig. 5a. Our simple model reproduces similar data, as shown in Fig. 4h and Fig. 5e by taking  $E_M = 3 \mu\text{eV}$  and keeping the other junction and dot parameters the same. This results in the characteristic zig-zag pattern in  $\sigma(C_Q)$  with peaks offset from each other by  $4E_M$ . In this regime, the observation of oscillations in both parity branches is unlikely, as can be seen in Fig. 5e. The qualitative agreement apparent between Fig. 5b and e suggests that scenario (b) is consistent with  $t_{m2} \sim t_{m1}$  and a moderate  $E_M$ . It is worth noting that this method enables us to probe the Majorana splitting energy  $E_M$  with single- $\mu\text{eV}$  resolution. This is a crucial parameter that characterizes the topological phase. Achieving a similar resolution for extracting  $E_M$  in transport measurements is quite challenging [87–89].

Lastly, scenario (c) is depicted in Fig. 5c. Here,  $C_Q$  exhibits bimodality but lacks flux-dependent oscillations. This observation is consistent with  $t_{m2} \gg t_{m1}$  and large  $E_M$ , as demonstrated in Fig. 5f. In this configuration, the interferometer loop is almost severed, leading to the absence of flux dependence in both parity branches. Despite this, the bimodality is still present due to non-zero  $E_M$ , as may be seen in Fig. 5f. If the loop were severed and  $E_M = 0$ , then the bimodality would disappear as well.

The changes we observe in the measured signal as a function of  $V_{\text{WP1}}$  can be attributed to changes in the properties of the low-energy state in the wire. We have fit our data to a model in which this state is assumed to be due to Majorana zero modes. However, the model can also be applied to a wire with a trivial low-energy

<sup>1</sup> Note that  $\sigma(C_Q)$  in Fig. 4d and the  $\Delta C_Q$  oscillations in Fig. 5b are suppressed for small  $B_{\perp}$  because the resonator frequency shifts with  $B_{\perp}$ , which leads to a reduction in SNR.

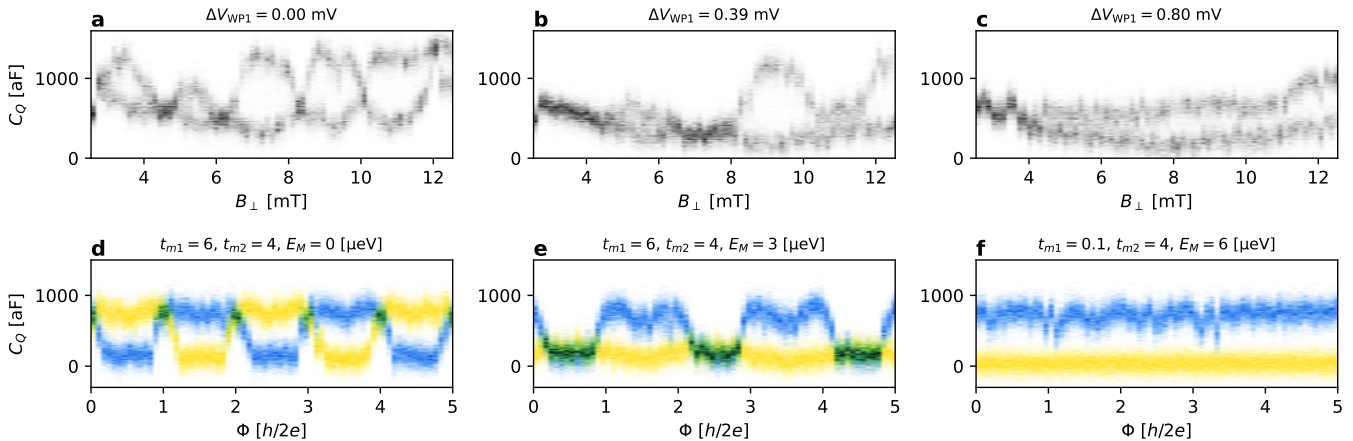


FIG. 5. Top row: Evolution of the histogram of resonator response values with voltage  $V_{WP1} = -1.8312 \text{ V} + \Delta V_{WP1}$ , which is a sampling of a dataset that has more closely-spaced  $V_{WP1}$  values. We use the same greyscale as in Fig. 2. Moving from left to right, panels a, b, and c exemplify scenarios a, b, and c described in the text. Each panel corresponds to a fixed charge transition of dot 2, typically the one with strongest signal. Bottom row: simulated data illustrating how this evolution can be understood in terms of the splitting of the fermionic mode  $E_M$  and the balancing of the couplings  $t_{m1}$ ,  $t_{m2}$ . Here, as in Fig. 4, blue and yellow indicate different total parities of the system. We have fixed  $t_{12} = t_{23} = 12 \mu\text{eV}$ ,  $N_{g1} = 0.7$  and  $N_{g3} = 0.35$  throughout. Moving from left to right, the MZM splitting  $E_M$  increases from 0 to 3 to 6  $\mu\text{eV}$ . Meanwhile the asymmetry between the left and right arms of the interferometer,  $t_{m2}/t_{m1}$ , is 1.5 in panels d and e and 40 in panel f.

Andreev state that has support at both ends of the wire. Such an accidental state could potentially appear outside the topological phase. In that part of the phase diagram, we interpret  $E_M$  as the energy of the accidental low-energy Andreev state. This splitting energy is generically large, with the exception of fine-tuned points. Moreover, the couplings to dot 1 and dot 3 will be imbalanced for an Andreev state that is localized near one of the ends of the wire. Within the topological phase, we expect a substantial variation in  $E_M$  in our current devices, attributable to mesoscopic fluctuations due to finite-size effects. Indeed, in the current generation of devices [48], we anticipate modest energy gaps  $\Delta_T$  and coherence lengths that are not significantly smaller than the device length. However, for devices with significantly higher  $\Delta_T$ , such variation in  $E_M$  is expected only at the boundaries of the topological phase where the system turns gapless. Conversely, deep within the topological phase, robust  $h/2e$ -periodic oscillations of  $\sigma(C_Q)$ , indicative of bimodality, should be observable.

## 5. DISCUSSION AND OUTLOOK

We have presented dispersive gate sensing measurements of the quantum capacitance in a topological qubit device designed for the readout of fermion parity shared between MZMs at the opposite ends of a nanowire. After tuning the nanowire density and in-plane magnetic field into the parameter regime where we expect the topological phase, and balancing the interferometer formed by the nanowire and the quantum dots, we observed

a flux-dependent bimodal RTS in the quantum capacitance. The long switching time of the RTS,  $\tau_{RTS} > 1 \text{ ms}$ , suggests a low quasiparticle poisoning rate in our devices at an in-plane magnetic field of approximately 2 T. This is consistent with the quasiparticle density measured in a Cooper pair box device. This interpretation can be further validated if  $\tau_{RTS}$  decreases when we intentionally inject quasiparticles into the device [46]. Taken together, these results are consistent with the measurement of the fermion parity of a near-zero-energy state in the nanowire. We have fit these data to a model in which the fermion parity is associated with two MZMs localized at the opposite ends of a 1DTS, but these measurements cannot, by themselves, determine whether the low-energy states detected by interferometry are topological. To resolve this issue, we will discuss the device's phase diagram and the stability of the observed flux-dependent RTS in a separate publication [46].

In conclusion, our findings represent significant progress towards the realization of a topological qubit based on measurement-only operations. The ability to perform single-shot fermion parity measurements is a key requirement for Majorana-based topological quantum computation architecture.

## ACKNOWLEDGMENTS

We thank Haim Beidenkopf, Sankar Das Sarma, Leonid Glazman, Bertrand Halperin, Angela Kou, Katherine Moler, Wolfgang Pfaff, and Mark Rudner for discussions. We thank Edward Lee and Todd Ingalls for

assistance with the figures. We are grateful for the contributions of Anand Dokania, Alexandra Efimovskaya, Linda Johansson, and Andrew Mullally at an early stage of this project. We have benefited from interactions with Paul Accisano, Parsa Bonderson, Jan Borovsky, Tom Brown, Gary Campbell, Srivatsa Chakravarthi, Kushal Das, Neil Dick, Raghu Gatta, Haris Gavranovic, Michael Goulding, Rachpon Kalra, Sarah Jablonski, Seth Kimes, Jamie Kuesel, Jason Lee, Jake Mattinson, Ali Moini, Tim Noonan, Diego Olivier Fernandez Pons, Len Sanderson, Marcus P. da Silva, Patrick Strøm-Hansen, Satoshi Suzuki, Matt Turner, Richard Yu, Andrew Zimmerman.

**Correspondence and requests for materials** should be addressed to Chetan Nayak (cnayak@microsoft.com).

<sup>†</sup>Morteza Aghaee, Alejandro Alcaraz Ramirez, Zulfi Alam, Rizwan Ali, Mariusz Andrzejczuk, Andrey Antipov, Mikhail Astafev, Amin Barzegar, Bela Bauer, Jonathan Becker, Alex Bocharov, Sridhi Boddapati, David Bohn, Jouri Bommer, Esben Bork Hansen, Leo Bourdet, Arnaud Bousquet, Samuel Boutin, Signe Brynold Markussen, Juan Carlos Estrada Saldaña, Lucas Casparis, Benjamin James Chapman, Sohail Chatoor, Cassandra Chua, Patrick Codd, William Cole, Paul Cooper, Fabiano Corsetti, Ajuan Cui, Juan Pablo Dehollain, Paolo Dalpasso, Michiel de Moor, Gijs de Lange, Andreas Ekefjård, Tareq El Dandachi, Saeed Fallahi, Luca Galletti, Geoff Gardner, Deshan Govender, Flavio Griggio, Ruben Grigoryan, Sebastian Grijalva, Sergei Gronin, Jan Gukelberger, Marzie Hamdast, Firas Hamze, Morten Hannibal Madsen, Jens Hedegaard Nielsen, Jens Munk Nielsen, Sebastian Heedt, Zahra Heidarnia, Jesús Herranz Zamorano, Samantha Ho, Laurens Holgaard, John Hornibrook, William Hvidtfelt Padkær Nielsen, Jinnapat Indrapiromkul, Henrik Ingerslev, Lovro Ivancevic, Jaspreet Jhoja, Jeffrey Jones, Konstantin V. Kalashnikov, Ray Kallaher, Farhad Karimi, Torsten Karzig, Evelyn King, Maren Elisabeth Kloster, Christina Knapp, Dariusz Kocon, Jonne Koski, Pasi Kostamo, Umesh Kumar Bhaskar, Mahesh Kumar, Tom Laeven, Thorvald Larsen, Kyunghoon Lee, Jason Lee, Grant Leum, Kongyi Li, Tyler Lindemann, Matthew Looij, Julie Love, Marijn Lucas, Roman Lutchny, Nash Madulid, Albert Malmros, Michael Manfra, Devashish Mantri, Esteban Martinez, Marco Mattila, Robert McNeil, Ryan V. Mishmash, Gopakumar Mohandas, Christian Mollgaard, Trevor Morgan, George Moussa, Chetan Nayak, Bas Nijholt, Mike Nystrom, Eoin O’Farrell, Thomas Ohki, Keita Otani, Brian Paquelet Wütz, Sebastian Pauka, Karl Petersson, Luca Petit, Dima Pikulin, Guen Prawiroatmodjo, Frank Preiss, Mohana Rajpalke, Craig Ranta, Katrine Rasmussen, David Razmadze, Outi Reentila, David J. Reilly, Yuan Ren, Ken Renneris, Antonio Rodolph Mei, Richard Rouse, Ivan Sadovskyy, Lauri Sainiemi, Irene Sanlorenzo, Emma Schmidgall, Cristina Sfiligoj, Mustafeez Bashir Shah, Kevin Simoes, Shilpi Singh, Sarat Sinha, Thomas Soerensen, Patrick Sohr, Tomas Stankevici, Lieuwe Stek, Eric Stuppard, Henri Suominen, Judith

Suter, Sam Teicher, Nivetha Thiyagarajah, Raj Tholapi, Mason Thomas, Emily Toomey, Josh Tracy, Michelle Turley, Shivendra Upadhyay, Ivan Urban, Kevin Van Hoogdalem, David J. Van Woerkom, Dmitrii V. Viazmitinov, Dominik Vogel, Georg W. Winkler, John Watson, Alex Webster, Joseph Weston, Anna Wulff Christensen, Chung Kai Yang, Emrah Yucelen, Roland Zeisel, Guoji Zheng, Justin Zilke

## Appendix A: Device design, fabrication and system setup

### 1. Device layout details

The qubit device shown in Fig. 6 is a practical realization of the linear tetron of Refs. 6 and 35. The complete device has 7 quantum dots, three long ones and four small ones. For concreteness, we call the long dots Dot 2, Dot 4, and Dot 6; the small dots are Dot 1, Dot 3, Dot 5, and Dot 7. Dots 2 and 6 run parallel to the two topological sections of the nanowire, and Dot 4 runs parallel to the middle trivial section of the nanowire. Each quantum dot is covered by a plunger gate in the second gate layer, whose purpose is to set the electrical potential on the underlying dot. We refer to the dot plunger gates using the convention “ $QDi$ ”. There are also “cutter” gates in the second gate layer. They cover the junctions: nanowire-Dot 1, Dot 1-Dot 2, Dot 2-Dot 3, Dot 3-nanowire, etc. as shown in Fig. 6a. Quantum dot cutter “ $QCi$ ” gates control inter-dot tunnel couplings; tunnel gates “ $TGi$ ” control coupling between the small dots and the nanowire; and source cutter “ $SCi$ ” gates control coupling between the small dots and the two-dimensional electron gas (2DEG) reservoirs. The 2DEG density in these reservoirs is set by the voltage on the helper gates “ $HGi$ ” which run from the dot region all the way to metallic Ohmic source contacts (denoted by purple boxes labeled “ $Si$ ” in Fig. 6a). The gates QD1, QD3, QD5, and QD7 are used to de-tune dot states from the Fermi energy, thereby setting the effective tunneling amplitudes of the MZMs from the wire to Dot 2, Dot 4, and Dot 6 via tunneling through the small dots. The lateral confinement of the dots is provided by the wire plunger “ $WPi$ ” gates and depletion gates “ $DGi$ ”.

The two topological wire segments (segments under WP1 and WP3) are 2.96  $\mu\text{m}$  long, and the trivial segment (segment under WP2) between them is 2.96  $\mu\text{m}$  long. Simulations of this device indicate that, in the topological phase, the coherence length has minimum value  $\xi = 1 \mu\text{m}$  [48], so  $e^{-L/\xi} \approx 0.05$ . The outer trivial segments (regions under side plungers SP1 and SP2) are 5  $\mu\text{m}$  long; hence, the topological segments are far from the normal electrons at the Ohmic contacts at the ends of the Al strip (drain contacts D1 and D2). The Al strip and, therefore, the nanowire beneath it is 60 nm wide, enabling full depletion of the InAs quantum well beneath the Al while providing sufficient screening of charged impurities in the dielectric.

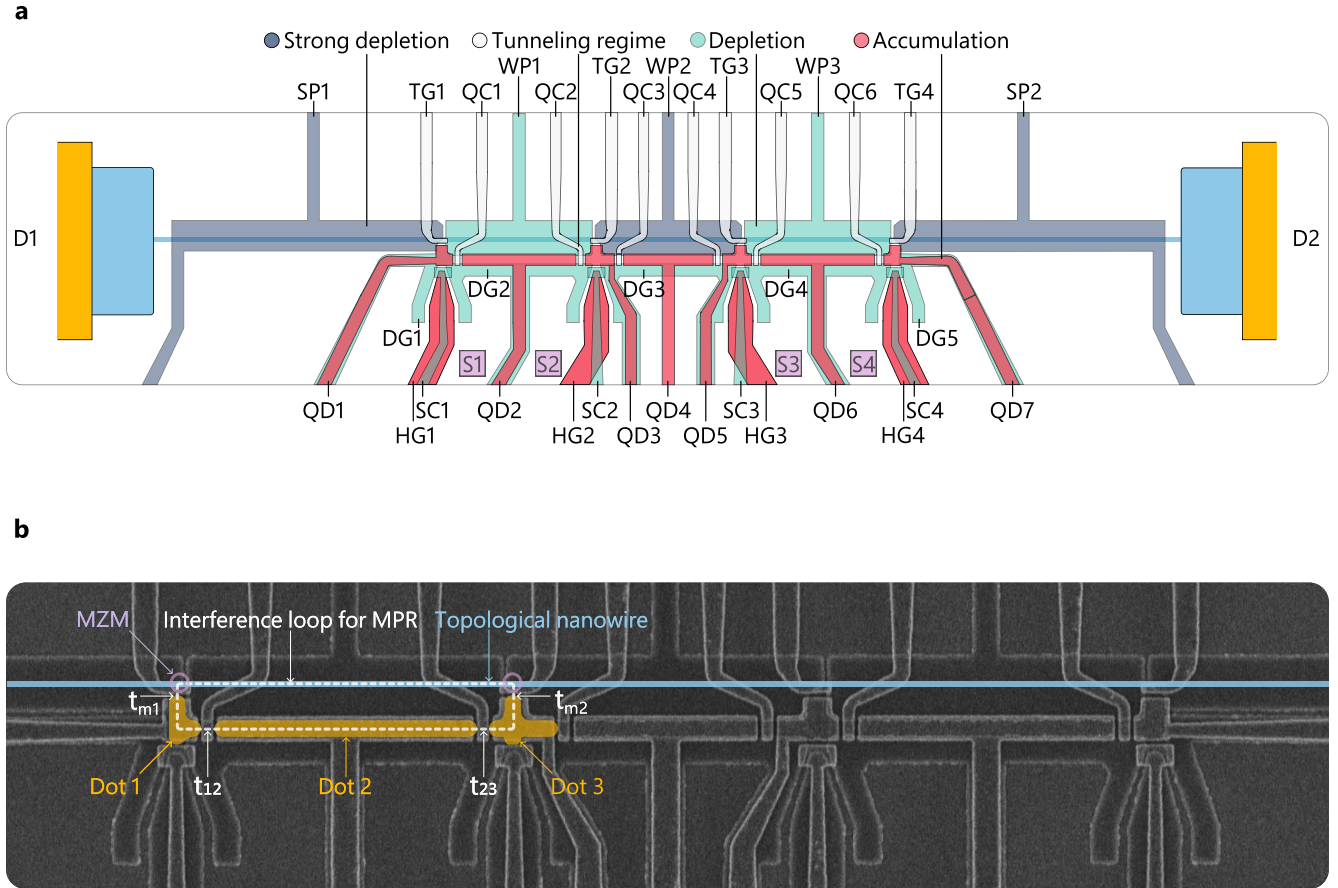


FIG. 6. (a) The gate layout of our device and voltage ranges necessary to form the interferometry loops needed for a functioning qubit device. Normal metal drain contacts (D1 and D2) are indicated in yellow. Normal metal source contacts S1-S4 are formed in 2DEG regions indicated by the purple boxes. The dark gray gates are normally set to very negative voltages  $V < -2.5$  V so that the quantum well is fully depleted underneath the gate, even underneath the aluminum strip (strong depletion). The teal gates are normally set to moderately negative voltages (between  $-2$  V and  $-1.5$  V) so that the quantum well is fully depleted underneath the gate, except underneath the aluminum strip (light blue), where the lowest sub-band is partially occupied (depletion). The white gates are set to voltages to form tunnel junctions and modulate the associated dot-nanowire or dot-dot tunnel coupling. The red gates are set to more positive voltages (accumulation). The corresponding gates can be seen in the SEM image in panel (b), where we have also marked the locations of the quantum dots, the MZMs, the tunneling paths between them, and the interference loop that links them all. Note that in the measurements presented in the main text, helper gates HG1 and HG2 are set to depletion to reduce the required voltages on SC1 and SC2 to isolate the loop, though this voltage setting is not required. Additionally, in the main text where the focus is on the left loop, the dot gates corresponding to the middle loop (QC3 and QD4) are fully depleted and the remaining gates on the right loop are grounded.

The small dots (dots 1, 3, 5, 7) have a T-junction shape with a width of 200 nm where they meet the cutter gates and an effective length between the nanowire and Dot 2 of 400 – 500 nm. The long dots (dots 2, 4, 6) are 2.4  $\mu$ m long. The cutter gates are 100 nm wide. These lengths were chosen so that Dot 2 could couple via Dot 1 and Dot 3 to the left topological segment's MZMs, which are  $\approx 3$   $\mu$ m apart; dots 1, 2, and 3 bridge this length. By breaking the length up in this way, we ensure that all dots have level spacings  $\gtrsim 10$   $\mu$ eV and dots 2, 4, and 6 have charging energy  $\gtrsim 45$   $\mu$ eV. Meanwhile, dots 1, 3, 5, and 7 have charging energy  $\gtrsim 100$   $\mu$ eV. Since the long dot level spacing is greater than the temperature, thermal smearing of the interference signal is minimized.

## 2. Device fabrication

The device presented here follows the same fabrication as dual-layer gate devices presented in the preceding work [48]. The 6.5 nm thick Al strip on top of the semiconductor substrate features larger Al pads at each end of length 1.5  $\mu$ m and width 3.5  $\mu$ m, see Fig. 6a. The Al pads are Argon milled to ensure low-resistance Ohmic contact to electron beam lithography defined structures of Ti(10 nm)/Au(140 nm)/Ti(10 nm) by which the Al strip is grounded. Both types of contacts are normal in the typical operating regime.

The Ti(2 nm)/Au(15 nm)/Ti(2 nm)/Al(10 nm) Gate layer 1 is separated from the semiconductor by Dielec-

tric 1 which consists of  $\approx 2$  nm  $\text{AlO}_x$  and 10 nm  $\text{HfO}_x$ . The electron beam lithography-defined gates in the first gate layer define the nanowire by depleting the 2DEG around the Al strip and also the quantum dots. The Ti(10nm)/Au(60nm) Gate layer 2 is separated from Gate 1 by Dielectric 2 which is 15 nm  $\text{AlO}_x$ . Layer 2 gates, also patterned by electron beam lithography, enable independent control of the coupling between the nanowire and quantum dots as well as the chemical potential of the quantum dots.

### 3. Superconductor-semiconductor hybrid heterostructure design

The heterostructure presented here is grown on commercially available semi-insulating InP wafers. A graded buffer is used to translate the lattice constant from that of InP, 0.587 nm, to one near InAs, 0.605 nm. The active region is constructed on the graded buffer and consists of a 25 nm  $\text{In}_{0.845}\text{Al}_{0.155}\text{As}$  lower barrier, a 9.1 nm thick InAs quantum well and a 6 nm thick  $\text{In}_{0.88}\text{Al}_{0.12}\text{As}$  top barrier, as well as the Al superconductor. The top barrier layer plays a critical role in fine-tuning the coupling between the superconductor and the 2DEG residing in the quantum well. For an Al parent gap which is  $\Delta_0 \sim 290 \mu\text{eV}$  in our device, we measure an induced gap  $\Delta_{\text{ind}} \sim 110 \mu\text{eV}$ . Another function of the top barrier layer is to separate the quantum well states from disorder on the dielectric-covered surface of the stack. From a Hall bar device simultaneously fabricated on the same chip as the nanowire device, we extract a peak mobility  $\mu \sim 75\,000 \text{ cm}^2/\text{Vs}$  at a density  $n_{\text{max}} \sim 1.2 \times 10^{12} \text{ cm}^{-2}$ .

Spin-orbit coupling strength in a hybrid superconductor-semiconductor structure is difficult to measure directly. Using weak anti-localization measurements in shallow InAs 2DEGs, see, for example, Ref. 90, and typical values of the electric field (obtained from simulations assuming the band offset parameter measured in Ref. 91), we estimate that the Rashba spin-orbit coupling is in the range of 5 to 15 meV·nm.

### 4. Readout system

The microwave readout chain is shown in Fig. 7. To measure fermion parity, the readout chain is designed to minimize the system noise temperature while maximizing the quasiparticle poisoning time  $\tau_{\text{qpp}}$ . To this end, we use a near-quantum limited amplifier, the JTWPA [62], as the first amplifier in the reflectometry setup. At the same time, low-pass and IR filters and several layers of shielding are applied to suppress stray radiation impinging on the sample. A table of key parameters characterizing the readout system is given in Table I.

$V_{\text{res}}$ [ $\mu\text{V}$ ]	$Q$	$\kappa_{\text{ext}}/2\pi$ [MHz]	$\omega/2\pi$ [MHz]	$C$ [fF]	$L_{\text{res}}$ [nH]	$T_{\text{N}}$ [K]	$\Delta C_Q$ [fF]
10(2)	35(4)	16(2)	617	580(25)	115	0.6(1)	1.0(2)

TABLE I. Measured parameters for the device shown in fig. 2, which are used to estimate the expected SNR.

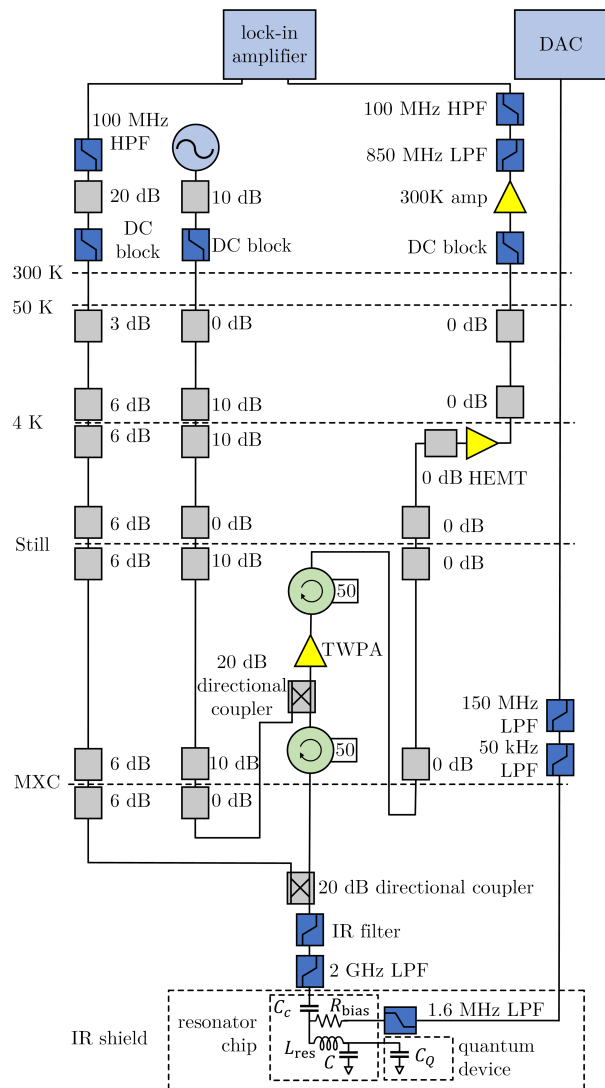


FIG. 7. Schematic diagram of the reflectometry setup used for the measurement of fermion parity by dispersive gate sensing, and shielding applied to sample, and filtering of rf and dc lines. The resonator chip includes a bias tee for setting  $V_{\text{QD2}}$ , through  $R_{\text{bias}} = 16\text{k}\Omega$ , and rf signal is routed to the capacitively coupled port, through  $C_c \sim 8\text{pF}$ , to the rest of the interferometry setup.

### 5. $C_Q$ conversion

To make connection with theory, we convert the measured microwave signal into a quantum capacitance  $C_Q$ . Previously,  $C_Q$  conversion has been performed with methods based on resonator fitting [61, 92]. These

can yield both the real and the imaginary parts of the quantum capacitance (also called the quantum conductance) [92]. Importantly, with the aid of a reference measurement composed of a frequency scan of the readout resonator, they allow conversion of a single IQ pair into a complex quantum capacitance.

Here we use a similar technique, which leverages symmetries and a small parameter expansion to obtain an analytical approximation for the mapping between the microwave signal and quantum capacitance. As in Refs. [61, 92], the first step in the conversion process is to determine the change in the resonance frequency  $\delta\omega_r$  and the loss rate  $\delta\kappa_{\text{int}}$  relative to the reference trace.

We first describe how the change in the resonance frequency  $\delta\omega_r$  is detected. After correction of electrical delay, the microwave reflection  $S_{11}$  of a readout resonator with resonant frequency  $\omega_r$ , internal loss rate  $\kappa_{\text{int}}$ , external loss rate  $\kappa_{\text{ext}}$ , and total linewidth  $\kappa = \kappa_{\text{int}} + \kappa_{\text{ext}}$  is

$$S_{11} = 1 - \frac{2\kappa_{\text{ext}}/\kappa}{1 + 2i(\omega - \omega_r)/\kappa}, \quad (\text{A1})$$

when it is probed at a frequency  $\omega$ . Crucially, Eq. (A1) depends on  $\omega$  and  $\omega_r$  only through their difference  $\omega - \omega_r$ . This implies that the change in  $S_{11}$  from a small shift in  $\omega_r$  is identical to the change resulting from an equal and opposite detuning of the probe frequency  $\omega$ . (Formally the shift in  $\omega_r$  needs not be small, but in practice non-idealities like the background ripple in the reflectometry setup or uncorrected electrical delay break the symmetry on which this argument rests.) The reference trace of  $S_{11}$  as function of the probe frequency  $\omega$  provides a look-up table of the reflection coefficients measured at different detunings. To determine the shift in the resonance frequency, we identify the point on the reference trace nearest to the IQ pair to be converted (which is probed at frequency  $\omega_r$ ). The detuning of this point from the resonance frequency in the reference trace is equal and opposite to the desired frequency shift  $\delta\omega_r$ . This process is illustrated in Fig. 8. The green disc indicates the IQ pair to be converted. An orange line of length  $\delta S_{11}^{\text{rad}}$  connects it to the nearest point on the circle, which has a known detuning that can be read from the colorbar.

To determine the change in the loss rate  $\kappa_{\text{int}}$  we leverage the fact that both  $\delta\omega_r/\kappa$ ,  $\delta\kappa_{\text{int}}/\kappa \ll 1$ . By expanding Eq. (A1) to first order in these small parameters, we determine their effect on the reflection coefficient:

$$\delta S_{11} \approx 2 \frac{\kappa_{\text{ext}}}{\kappa} \left( \frac{\delta\kappa_{\text{int}}}{\kappa} - 2i \frac{\delta\omega_r}{\kappa} \right). \quad (\text{A2})$$

In Eq. (A2),  $\delta\kappa_{\text{int}}$  changes the real part of  $S_{11}$ . Geometrically this corresponds to a radial translation toward or away from the circle that the reference trace forms in the IQ plane. For this reason we denote the distance between the circle of the reference trace and the IQ pair to be converted as  $\delta S_{11}^{\text{rad}}$  (see Fig. 8). As with the determination of  $\delta\omega_r$ , here again the reference trace can be used as a

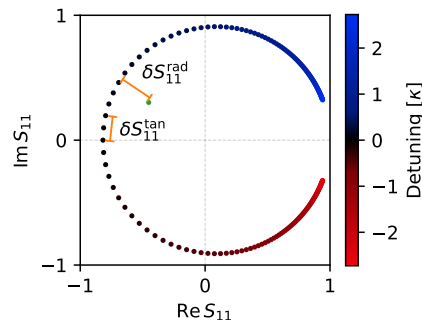


FIG. 8. Geometrical depiction of the  $C_Q$  conversion process for an IQ pair with  $\delta\omega_r = \kappa/8$ ,  $\delta\kappa_{\text{int}} = \kappa/5$ . The circle shows the reflection of an overcoupled resonator in IQ space. The green disc represents a sample IQ pair to be converted into a complex  $C_Q$ . The real (imaginary) component of  $C_Q$  encodes  $\delta\omega_r$  ( $\delta\kappa_{\text{int}}$ ) and causes translations along the arc (radius) of the circle.

look-up table to read off the translation in IQ space  $\delta S_{11}^{\text{tan}}$  from a small (relative to  $\kappa$ ) detuning  $\delta\omega$ . (We denote the translation with the superscript ‘tan’ because it is tangential to the circle of the reference trace.) The change in the loss rate is then

$$\delta\kappa_{\text{int}} \approx 2 \frac{\delta\omega}{\delta S_{11}^{\text{tan}}} \delta S_{11}^{\text{rad}}. \quad (\text{A3})$$

In practice, selection of  $\delta\omega$  involves a tradeoff—it should be chosen to be as large as possible (to reduce inaccuracies from readout noise) while also being much less than the linewidth  $\kappa$  (to reduce inaccuracies from the series expansion). We choose  $\delta\omega \approx \kappa/20$ .

Finally, to convert the computed complex frequency shifts into a complex quantum capacitance  $C_Q$  we use the fact that  $C_Q$  is small relative to the total capacitance  $C$ . Expanding  $\omega_r = 1/\sqrt{L_{\text{res}}(C + C_Q)}$  we have

$$\frac{K}{\omega_r} = -\frac{1}{2} \frac{C_Q}{C} + \mathcal{O}\left(\frac{C_Q}{C}\right)^2. \quad (\text{A4})$$

Here  $K = \delta\omega_r - i\delta\kappa_{\text{int}}/2$  denotes the complex response of the system (see also Appendix B), the real part of which encodes the shift in the resonance frequency. Following convention, the imaginary part encodes  $-\kappa_{\text{int}}/2$ , such that a positive  $\text{Im } C_Q$  corresponds to an increase in  $\kappa_{\text{int}}$ . We therefore have

$$\begin{aligned} \frac{\mathcal{R}[C_Q]}{C} &= -2 \frac{\delta\omega_r}{\omega_r}, \\ \frac{\mathcal{I}[C_Q]}{C} &= \frac{\delta\kappa_{\text{int}}}{\omega_r}. \end{aligned} \quad (\text{A5})$$

The capacitance  $C$  is computed with knowledge of the inductance  $L_{\text{res}}$  on the resonator chip and resonance frequency,  $C \approx (\omega_r^2 L_{\text{res}})^{-1}$ .

We conclude this section with a practical note: measuring the IQ pair to be converted with a probe frequency  $\omega \neq \omega_r$  leads to conversion inaccuracy from the

microwave background non-idealities. To remedy that, the IQ data can be transformed before performing the  $C_Q$  conversion procedure. This transformation starts by rotating around the center of the resonance circle in IQ space by  $\arg S_{11}(\omega_r) - \arg S_{11}(\omega)$ . The center of the circle can be determined by fitting an arc near resonance using an algebraic fit, such as Pratt's method [93]. The data is then scaled by the ratio of point densities  $\delta\omega/\delta S_{11}^{\text{tan}}$  at  $\omega_r$  and  $\omega$  to account for the frequency-dependent phasal density of IQ pairs. Furthermore, the properties of the resonator may shift slightly with changes in the magnetic field. Here, we have chosen to use the same reference trace for all values of the out-of-plane field  $B_{\perp}$ , which may lead to a slow, systematic change of the extracted  $C_Q$  over the field range. This can be seen, e.g., in Fig. 2b in the small overall curvature of the lower  $C_Q$  branch. Noting that  $C_Q$  is a state-dependent shift of the full circuit capacitance, and as such is defined only up to an additive constant, we use this freedom to set the  $C_Q$  deep in the Coulomb valley to 0 in some figures to improve the clarity of presentation, such as Fig. 4.

## Appendix B: Theoretical model

### 1. Basic features of the device design

In the topological superconducting phase of a nanowire, the low-energy physics is characterized by two real fermionic operators  $\gamma_1$  and  $\gamma_2$ . These operators are localized at the left and right ends of the topological section, respectively, and satisfy the relationship  $\{\gamma_i, \gamma_j\} = 2\delta_{ij}$ . The wire has two nearly-degenerate ground states with opposite fermion parities  $i\gamma_1\gamma_2 = \pm 1$ . The splitting energy between these states,  $E_M$ , is approximately  $E_M \sim \Delta_T \exp(-L/\xi)$  in the limit where  $L \gg \xi$  [15]. Here,  $\xi$  represents the coherence length, and  $\Delta_T$  is the topological gap. This behavior holds also in the presence of disorder [94], although the coherence length  $\xi$  is renormalized [95].

To measure the parity of Majorana zero modes (MZMs), we designed a device with three quantum dots (QDs) and a readout resonator. The middle QD (dot 2) is coupled to the resonator, while the side QDs (dot 1 and dot 3) act as tunable barriers. We show that the tunneling rate between dot 2 and the nanowire depends on the detuning energies in dot 1 and dot 3. We then

derive a low-energy model for this system and estimate the quantum capacitance signal.

### 2. Effective Hamiltonian for MZM-dot 1-dot 2 system

We now develop an effective low-energy model for the MZM-dot 1-dot 2 system. This model facilitates the determination of the effective parameters in Eq. (1), and it elucidates the distinction between balanced and unbalanced interferometers. The Hamiltonian for the MZM-dot 1-dot 2 system is given by

$$H = 2E_M \left( c^\dagger c - \frac{1}{2} \right) + \Delta_1 \left( f^\dagger f - \frac{1}{2} \right) + \Delta_2 \left( d^\dagger d - \frac{1}{2} \right) + H_t \quad (\text{B1})$$

$$H_t = t_{m1} f^\dagger (c + c^\dagger) + t_{m1}^* (c + c^\dagger) f + t_{12} f^\dagger d + t_{12}^* d^\dagger f$$

Here, we introduce non-local fermionic operators in the wire, denoted as  $c = (\gamma_1 + i\gamma_2)/2$  and  $c^\dagger = (\gamma_1 - i\gamma_2)/2$ . These operators encode the fermion occupation of a pair of Majorana zero modes, with Majorana splitting energy denoted by  $E_M$ . The operators  $f^\dagger$ ,  $f$  and  $d^\dagger$ ,  $d$  are fermion creation and annihilation operators in the small (e.g., dot 1) and long (dot 2) quantum dots, respectively. The detuning of quantum dots  $i$  from the degeneracy point is given by  $\Delta_i(N_{gi}) = E_{Ci}(1 - 2N_{gi}) + \delta_i$ . The parameters  $E_{Ci}$ ,  $N_{gi}$  and  $\delta_i$  denote the charging energy, dimensionless offset charge, and level spacing of the  $i$ -th dot, respectively. The dimensionless offset charge is controlled by the gate voltage, expressed as  $N_{gi} = \alpha_i e V_{\text{QDi}} / (2E_{Ci})$ , where the lever arm  $\alpha_i = 2C_{gi}E_{Ci}/e^2$ . We assume that the level spacing in the quantum dots is large  $\delta_i \gg k_B T, |t_{12}|, |t_{m1}|$  ( $T$  being temperature), thereby enabling an effective description via a single-level approximation. Lastly, the matrix elements  $t_{m1}$  and  $t_{12}$  describe the tunneling between dot 1-MZM and dot 2-dot 1, respectively.

Let us first focus on the even parity sector of the combined MZM-dot 1-dot 2 system and derive the effective Hamiltonian when dot 1 is detuned from resonance. We use the basis convention  $|a, b, c, d\rangle = |0, 1, 0, 1\rangle_{\text{MZM}} \otimes |0, 0, 1, 1\rangle_{\text{QD1}} \otimes |0, 1, 1, 0\rangle_{\text{QD2}}$ . The corresponding Hamiltonian is given by

$$H_{\text{even}} = \begin{pmatrix} -E_M - \frac{\Delta_1}{2} - \frac{\Delta_2}{2} & 0 & 0 & -t_{m1}^* \\ 0 & E_M - \frac{\Delta_1}{2} + \frac{\Delta_2}{2} & t_{m1}^* & t_{12}^* \\ 0 & t_{m1} & -E_M + \frac{\Delta_1}{2} + \frac{\Delta_2}{2} & 0 \\ -t_{m1} & t_{12} & 0 & E_M + \frac{\Delta_1}{2} - \frac{\Delta_2}{2} \end{pmatrix} \quad (\text{B2})$$

The above Hamiltonian can be simplified in the limit

of large dot 1 detuning. Assuming that  $|\Delta_1| \gg$

$|\Delta_2|, |t_{m1}|, |t_{12}|, E_M$  we can perform a Schrieffer–Wolff

transformation and ‘integrate out’ dot 1 to arrive at

$$\tilde{H}_{\text{even}} = \begin{pmatrix} -E_M - \frac{\Delta_1}{2} - \frac{\Delta_2}{2} - \frac{|t_{m1}|^2}{\Delta_1} & \frac{t_{12}t_{m1}^*}{\Delta_1} & 0 & 0 \\ \frac{t_{12}^*t_{m1}}{\Delta_1} & E_M - \frac{\Delta_1}{2} + \frac{\Delta_2}{2} - \frac{|t_{m1}|^2 + |t_{12}|^2}{\Delta_1} & 0 & 0 \\ 0 & 0 & -E_M + \frac{\Delta_1}{2} + \frac{\Delta_2}{2} + \frac{|t_{m1}|^2}{\Delta_1} & \frac{t_{12}^*t_{m1}}{\Delta_1} \\ 0 & 0 & \frac{t_{12}t_{m1}^*}{\Delta_1} & E_M + \frac{\Delta_1}{2} - \frac{\Delta_2}{2} + \frac{|t_{m1}|^2 + |t_{12}|^2}{\Delta_1} \end{pmatrix} \quad (\text{B3})$$

In this derivation, we have disregarded small terms of  $O(1/|\Delta_1|^2)$ . The upper left block is representative of an empty dot 1 (i.e., when  $\Delta_1 > 0$ ), while the lower right block is for an occupied dot 1 (i.e., when  $\Delta_1 < 0$ ). The off-diagonal terms within each sub-block correspond to co-tunneling through dot 1. Consequently, the side dots essentially facilitate a tunable MZM-dot 2 coupling. Furthermore, tunneling between dot 2-dot 1 and dot 1-MZM leads to a correction of detuning energies. It’s important to note that these corrections, induced by quantum fluctuations, differ for empty and occupied dot 2 states. Consequently, as shown below, the peak of the quantum capacitance experiences a shift with respect to the  $\Delta_2 = 0$  line even when  $E_M = 0$ .

An analogous analysis can be performed for the odd parity sector of the combined MZM-dot 1-dot 2 subsystem. In the appropriate basis, the effective Hamiltonian  $\tilde{H}_{\text{odd}}$  can be derived from  $\tilde{H}_{\text{even}}$  by substituting  $E_M$  with  $-E_M$ . The quantum capacitance for a state  $n$  with energy  $\varepsilon_n$  can be expressed as  $C_Q^{(n)} = -e^2\alpha^2 \partial^2 \varepsilon_n / \partial E_D^2$ . Assuming thermal occupation, the quantum capacitance for even and odd parity sectors reads:

$$C_Q(Z) = \frac{e^2\alpha^2 2|t_{\text{eff}}|^2}{[(E_D + Z2E_M)^2 + 4|t_{\text{eff}}|^2]^{3/2}} \times \tanh\left(\frac{\sqrt{(E_D + Z2E_M)^2 + 4|t_{\text{eff}}|^2}}{2k_B T}\right) \quad (\text{B4})$$

where  $E_D = \Delta_2 - \frac{|t_{12}|^2}{|\Delta_1|}$  and  $t_{\text{eff}} = \frac{t_{12}t_{m1}^*}{\Delta_1}$  and  $Z = \pm 1$  for even/odd parity states of the combined MZM-dot 1-dot 2 subsystem. The temperature dependence is due to thermal occupation of the excited state within each parity sector, which suppresses  $C_Q$ . In the interferometer setup, when dot 2 is coupled to both MZMs, one obtains Eq. (1), where the effective parameters are given by the expressions above.

### 3. Dynamical response of the TQDI within linear response theory

In this section, we calculate the dynamical response of the TQDI coupled to a readout resonator. By extending

the effective model derived earlier to the MZM-dot 1-dot 2-dot 3-MZM setup, we arrive at the following effective Hamiltonian:

$$H_F = E_D d^\dagger d + 2E_M \left(c^\dagger c - \frac{1}{2}\right) + t_R d^\dagger (c + c^\dagger) + t_R^* (c + c^\dagger) d + it_L d^\dagger (c^\dagger - c) + it_L^* (c^\dagger - c) d. \quad (\text{B5})$$

Here  $E_D = \Delta_2 - |t_{12}|^2/|\Delta_1| - |t_{23}|^2/|\Delta_3|$ ,  $t_L = t_{12}t_{m1}^*/\Delta_1$  and  $t_R = t_{23}t_{m2}^*/\Delta_3$ . The quantities  $\Delta_i (N_{gi}) = E_{Ci}(1 - 2N_{gi}) + \delta_i$  are the detunings of the quantum dots from their degeneracy points, as defined above. The couplings  $t_{m1}$  and  $t_{m2}$  denote QD-MZM couplings for dot 1 and dot 3, respectively, while  $t_{12}$ ,  $t_{23}$  describe tunneling between dot 1-dot 2 and dot 2-dot 3, respectively.

To perform a readout of the fermion parity split between  $\gamma_1$  and  $\gamma_2$ , we couple dot 2 to a readout resonator with an angular frequency  $\omega_r$ . In the rotating frame, the full Hamiltonian, including the microwave photons, is given by

$$H = H_F + (\omega_r - \omega)\hat{a}^\dagger \hat{a} + g d^\dagger d (\hat{a} e^{-i\omega t} + \hat{a}^\dagger e^{i\omega t}). \quad (\text{B6})$$

Here  $a^\dagger$  and  $a$  denote the photon creation and annihilation operators in the resonator, and the coupling to the resonator is defined as  $g = \alpha_2 e \sqrt{\hbar\omega_r/2C}$  where  $C$  is the total effective capacitance of the readout circuit, which includes the capacitance of the resonator itself.

To understand the impact of a quantum device on the resonator, it is necessary to calculate both the frequency shift and the system-induced loss on the photon degrees of freedom. This can be achieved by integrating out the fermionic degrees of freedom. Upon performing this procedure and retaining only the lowest-order corrections in  $g$ —an approach equivalent to linear response theory—one finds that the resonator’s response is encapsulated in the following correlation function:

$$K^R(\omega) = -i \frac{g^2}{2} \int \frac{d\omega_1}{2\pi} \text{Tr} \left[ \hat{V} G^K(\omega_1) \hat{V} G^R(\omega_1 + \omega) + \hat{V} G^A(\omega_1) \hat{V} G^K(\omega_1 + \omega) \right]. \quad (\text{B7})$$

Here  $G^R(\omega)$ ,  $G^A(\omega)$  and  $G^K(\omega)$  denote the retarded, advanced and Keldysh Green’s functions, respectively, for

the Hamiltonian  $H_F$ . The vertex operators  $\hat{V}$  are defined as  $\hat{V} = \partial[C^R(\omega)]^{-1}/\partial E_D$ . The real and imaginary components of  $K^R(\omega)$  represent the shift in the resonator frequency and photon loss, respectively. The response of the system can be interpreted as a dynamical quantum capacitive shift  $C_Q(\omega)$  relative to the capacitance of the readout circuit  $C$  which we model by an effective lumped element circuit (see Fig. 1c). Expanding for  $C_Q(\omega) \ll C$  yields the relation

$$\frac{C_Q(\omega)}{2C} = -\frac{K^R(\omega)}{\omega_r}. \quad (\text{B8})$$

As  $\omega$  and  $T$  approach zero, the expression for  $C_Q(\omega)$  recovers the quantum capacitance of a ground state of the system.

Finally, by projecting the Hamiltonian Eq. (B5) onto both the even and odd parity sectors of the QD-wire system and utilizing Eq. (B7), we can derive an expression for the dynamical quantum capacitance of the TQDI within each parity sector:

$$\begin{aligned} \frac{C_Q(Z, \phi, \omega)}{2C_{\Sigma,2}} &= \frac{2\alpha^2 E_{C2} |t_C(Z, \phi)|^2}{\sqrt{(E_D + Z2E_M)^2 + 4|t_C(Z, \phi)|^2}} \\ &\times \frac{\tanh\left(\sqrt{(E_D + Z2E_M)^2 + 4|t_C(Z, \phi)|^2}/2T\right)}{(E_D + Z2E_M)^2 + 4|t_C(Z, \phi)|^2 - (\omega + i\eta)^2}, \end{aligned} \quad (\text{B9})$$

where  $C_{\Sigma,2}$  is the total capacitance of dot 2, while  $\eta$  is the broadening of the resonance due to the coupling to the environment (see also the discussion below). The term  $t_C(Z, \phi)$  in Eq. (B9) is given by

$$|t_C(Z, \phi)|^2 = |t_L|^2 + |t_R|^2 + 2Z|t_L||t_R|\sin\phi. \quad (\text{B10})$$

Here,  $\phi$  is the phase difference between the left and right QD-wire junctions, which is controlled by the external magnetic flux, given by  $\phi = 2\pi\Phi/\Phi_0 + \phi_0$  with  $\Phi_0 = h/e$ .  $\phi_0$  is a flux-independent offset.  $C_Q$  for each parity sector exhibits periodicity in flux with period  $h/e$ . Both the real and imaginary parts of  $C_Q(Z, \phi, \omega)$  contain significant information regarding microscopic parameters, which can be used in comparing simulation to experiment.

The difference in the dynamical quantum capacitance between the even and odd parity sectors is given by

$$\Delta C_Q(\phi, \omega) = |C_Q(1, \phi, \omega) - C_Q(-1, \phi, \omega)| \quad (\text{B11})$$

In the static limit  $\omega \rightarrow 0$ , one recovers Eq. (3) of the main text. Using Eq. (B9), we estimate that the maximum value of  $|\Delta C_Q|$  is approximately 1 fF using the parameters  $E_M = 1 \mu\text{eV}$ ,  $t_R = 3 \mu\text{eV}$ ,  $t_L = 3 \mu\text{eV}$ ,  $\eta = 1 \mu\text{eV}$ ,  $T = 5 \mu\text{eV}$ ,  $\omega = 2 \mu\text{eV}$ ,  $E_{C2} = 45 \mu\text{eV}$ ,  $\alpha = 0.5$ . As discussed in the main text (see Sec. 3), the peaks in  $\Delta C_Q(\phi, \omega)$  for even and odd parities occur at  $E_D = -2E_M$  and  $E_D = 2E_M$ , respectively. As  $E_M$  increases, at  $E_D = -2E_M$ ,  $C_Q$  is suppressed in the odd parity sector and enhanced in the even parity sector, and vice versa at  $E_D = 2E_M$ .

Lastly, it is useful to introduce an index,  $\nu$ , which tracks parity of the ground state in the interferometer configuration as a function of flux. The Hamiltonian, defined in Eq. (B5), can be expressed in the Majorana basis as  $H_F = \sum_{i,j} A_{ij}(\phi) i\gamma_i \gamma_j$ , where  $A_{ij}(\phi)$  is a real skew-symmetric matrix. As follows from Ref. [15], the change in fermion parity in the ground state is represented by

$$\nu = \text{sign Pf}[A_{ij}(\phi)] \text{Pf}[A_{ij}(\phi + \pi)]. \quad (\text{B12})$$

For the model represented by Eq. (B5), one finds that the expression for  $\nu$  becomes

$$\nu = \text{sign}[(E_D E_M)^2 - 4|t_L|^2 |t_R|^2 \sin^2 \phi]. \quad (\text{B13})$$

From this expression, it follows that when  $E_M$  is finite, a large detuning energy could potentially lead to a change in fermion parity within the loop configuration. This is not surprising because in a loop configuration we essentially perform a non-local measurement of the fermion parity encoded in Majorana zero modes (MZMs). To mitigate the backaction of the measurement, which may change the fermion parity of the system's ground-state, it is crucial to maximize the couplings  $t_R$ ,  $t_L$  and to minimize both  $E_M$  and  $E_D$ . This establishes a requirement for  $E_M \ll \min(2|t_L||t_R|/|E_D|, \Delta_T)$ . The second term on the right-hand-side arises from the requirement that  $E_M$  must be much smaller than the topological gap  $\Delta_T$ .

#### 4. Dynamical $C_Q$ calculation using open system dynamics

The linear response theory outlined above provides an intuition for how the dynamical  $C_Q$  response arises in our setup. For quantitative comparison to the experimental data, it is important to capture larger drive amplitudes beyond linear response. We therefore use a different approach that is based on simulating the dynamics of the system in an open-system framework. We first note that in typical dispersive gate sensing setups, the resonator photons are well-described by the classical limit  $\hat{a} \rightarrow a$  of a large number of photons. This can be used to reduce Eq. (B6), or its generalization including all 3 QDs explicitly, to a time-dependent problem in the fermionic Hilbert space. Specifically, the coupling to the (classical) photon fields can be captured via

$$\tilde{H}_F = H_F + 2g|a|d^\dagger d \cos(\omega t). \quad (\text{B14})$$

The equation of motion of the classical field  $a$  takes the form

$$\dot{a} = i[\omega - \omega_r - K(\omega)]a - \frac{\kappa}{2}a - \sqrt{\kappa_e}b_{\text{in}}, \quad (\text{B15})$$

where  $K(\omega) = g\langle d^\dagger d \rangle(t)e^{i\omega t}/|a|$  and we included photon decay  $\kappa = \kappa_{\text{ext}} + \kappa_{\text{int}}$  due to internal loss  $\kappa_{\text{int}}$  and coupling to the readout line  $\kappa_{\text{ext}}$  and the external drive  $b_{\text{in}}$  via standard input-output theory, see e.g. Ref. [96].

We then solve the equations Eq. (B14) and Eq. (B15) including the effects of a noisy environment using the Universal Lindblad master equation (ULE) approach described in Ref. [97] where  $\langle d^\dagger d \rangle(t) = \text{tr}\{\rho(t)d^\dagger d\}$  with the density matrix  $\rho(t)$  obtained for the corresponding ULE with Hamiltonian Eq. (B14). This approach allows us to numerically simulate the dynamical  $C_Q$  response of the MZM-dot 1-dot 2-dot 3-MZM system including the backaction from the finite drive amplitude. The dissipative terms in the ULE formalism naturally lead to the imaginary part of the response captured by the phenomenological parameter  $\eta$  in the linear response theory Eq. (B9). For a more detailed description of this approach to determining the rf response of the system as well as a detailed comparison to the linear response regime, see Ref. [98].

### a. Quantum Noise

In this framework, the various noise channels through which the environment couples to the system can be specified via a set of system operators  $X_i$  and noise spectral functions  $S_i(\omega)$ . They can capture charge noise, phonon noise and other noise sources. For the purpose of simulating a system that is driven by the resonator, it is essential to capture the coupling to a low-temperature environment which leads to a steady state that is close to thermal equilibrium. The condition that the environment is in thermal equilibrium can be stated in terms of the spectral functions as  $S_i(\omega)/S_i(-\omega) = \exp(\hbar\omega/k_B T)$ .

### b. Treatment of low-frequency charge noise

An important contributor to the detuning noise of QDs is  $1/f$  charge noise which is particularly strong at low frequencies. Due to the long-time correlations of this noise it cannot easily be described via the spectral functions of the ULE framework. Instead, we capture this noise by making use of the ability to handle arbitrary time dependence of the Hamiltonian  $\hat{H}_F$  and treat the low-frequency charge noise explicitly as classical noise on the corresponding terms in the Hamiltonian. This approach has been used previously, e.g. in Ref. [99], and we follow the approach discussed there to generate an ensemble of noise trajectories. While in principle, this approach requires repeating the time evolution for many different noise realizations, we find that in many practical situations it is sufficient to consider noise on the timescale of the measurement. Since the evolution is completely adiabatic with respect to that scale, a simplified approach can be used, as discussed in Appendix D.

## 5. Expected signal-to-noise ratio

To estimate the expected Signal-to-Noise ratio (SNR) of the measurement of  $\Delta C_Q$  we consider the steady state

solution of Eq. (B15)

$$a = \frac{\sqrt{\kappa_{\text{ext}}} b_{\text{in}}}{i(\omega - \omega_Z) - i\kappa/2} \quad (\text{B16})$$

where  $\omega_Z = \omega_r + K(\omega, Z)$ . Within standard input-output theory, the relation between the incoming and outgoing photon fields is given by  $b_{\text{out}} = b_{\text{in}} + \sqrt{\kappa_{\text{ext}}} a$  [96]. The relevant signal  $S = |b_{\text{out},+1} - b_{\text{out},-1}|/2$  is then given by the shift of the output fields relative to each other. The typical frequency shift  $|\omega_{+1} - \omega_{-1}|$  in our devices is small compared to  $\kappa$  which allows for an expansion of the signal to lowest order in the capacitive shift,

$$S = \frac{\sqrt{\kappa_{\text{ext}}} |a| \omega_0}{2\kappa C} \Delta C_Q \quad (\text{B17})$$

where we used the regime of optimal drive frequency  $\omega = (\omega_{+1} + \omega_{-1})/2$ . Recasting this in terms of the voltage amplitude  $V_{\text{res}} = \sqrt{2\hbar\omega_r/C}|a|$  in the resonator and adding noise from an amplification chain of effective noise temperature  $T_N$ , the signal to noise ratio is given by

$$\text{SNR} = V_{\text{res}} \frac{Q}{2} \sqrt{\frac{\kappa_{\text{ext}} \tau_m}{C k_B T_N}} \Delta C_Q \quad (\text{B18})$$

where  $Q = \omega_r/\kappa$  and  $\tau_m$  is the integration time of the measurement.

Eq. (B18) appears to yield an SNR that is monotonically increasing with  $V_{\text{res}}$ . However, the SNR is, in fact, limited by backaction. As  $V_{\text{res}}$  increases, power broadening will decrease the dynamical  $\Delta C_Q$  which yields an optimum in the drive amplitude which is typically of the order  $e\alpha V_{\text{res}} \sim (2t_C - \hbar\omega)$ . Note that the dynamical  $C_Q$  formalism outlined above can capture this backaction via Eq. (B14) and Eq. (B15).

We now estimate a typical SNR in our setup using the parameters in Table I. These parameters are obtained with measurements on the same device shown in Fig. 2. Using Eq. (B18), we estimate  $\text{SNR} = 0.8(2)$  in  $\tau_m = 1 \mu\text{s}$ . Fig. 9 shows the SNR extraction for the time trace depicted in Fig. 2d. We find  $\text{SNR} = 0.52$  in  $\tau_m = 1 \mu\text{s}$ , which is comparable to the estimated SNR value and allows  $\text{SNR} = 1$  to be obtained in  $\tau_m = 3.7 \mu\text{s}$  of integration time. We conclude that the sizable capacitive shifts enable fast single-shot readout even with relatively low- $Q$  resonators. Our result compares favorably with the single-shot readout of gate-based spin qubits with off-chip resonators demonstrated in Refs. 100–102.

In the context of measurement-based quantum computation, an important performance metric is the probability of assignment errors, which needs to take into account the probability of state flips during the measurement. To this end, we define this quantity as

$$p_{\text{err}} = \left[ 1 - e^{-\tau_m/\tau_{\text{qpp}}} \text{erf} \left( \text{SNR}(\tau_m)/\sqrt{2} \right) \right] / 2. \quad (\text{B19})$$

Assuming  $\tau_{\text{qpp}} = 2 \text{ ms}$  and the SNR extracted above, we find an optimal measurement time of  $32.5 \mu\text{s}$  and a corresponding  $p_{\text{err}} \approx 1\%$ . We note that this is the optimal

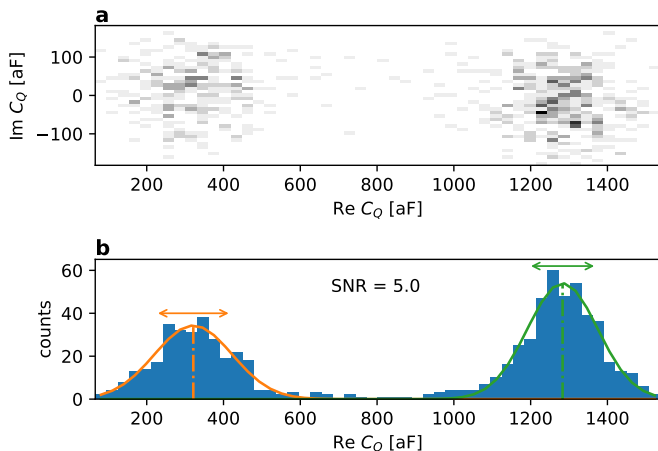


FIG. 9. SNR extraction of the time trace shown in Fig. 2d. (a) Raw rf signal converted to complex  $C_Q$  by the method described in Appendix A 5. We applied an overall shift to center  $\text{Im } C_Q$  of the data around zero. (b) Histogram of  $\text{Re } C_Q$  with Gaussian fits. The distributions are centered around  $\overline{C_{Q,+}} = 321 \text{ aF}$  and  $\overline{C_{Q,-}} = 1283 \text{ aF}$ , with standard deviations  $\text{std}[C_{Q,+}] = 101 \text{ aF}$  and  $\text{std}[C_{Q,-}] = 92 \text{ aF}$ . These are indicated by the orange (green) dash-dotted lines and arrows, respectively. The SNR is given by  $|\overline{C_{Q,+}} - \overline{C_{Q,-}}| / (\text{std}[C_{Q,+}] + \text{std}[C_{Q,-}]) = 5.0$  for an effective integration time of  $91 \mu\text{s}$ . The slight difference in standard deviation as well as height of the Gaussians can be attributed to the finite sample size used for fitting.

measurement time at optimal flux, whereas for other flux values a longer measurement time is better able to distinguish the parity sectors. For this reason, we have used a longer measurement time throughout this paper.

### Appendix C: Device tune-up

This section describes the general procedure to tune up the left TQDI loop in order to perform the interferometry measurements described in the main text. A similar procedure can be used to tune up the right TQDI loop.

Device tune-up requires both dc transport and rf dispersive gate sensing measurements. We first perform coarse tuning of quantum dots separated from the wire to the appropriate configuration satisfying the requirements described in Appendix A 1. In this step, each individual dot is formed separately and the rf drive is calibrated. After tuning the dots individually, the triple quantum dot system is tuned via dispersive gate sensing. As a next step, we use the dc transport measurements that comprise the topological gap protocol (TGP) [48] to tune the nanowire into the relevant parameter regime in terms of wire plunger and in-plane magnetic field where we expect the topological phase. Finally, we proceed to tune the interferometer to optimize the  $\Delta C_Q$  signal.

## 1. Pre-TGP wire transport

First, the Ohmic contacts S1 and S2 are isolated from one another and the other Ohmic contacts by setting depletion gates DG1, DG2, and DG3 and cutters QC1 and QC2 below their respective threshold voltages. In this configuration, the depletion voltage, induced gap, and parent gap of the topological wire segment are measured using local and non-local conductance spectroscopy as described in Ref. 48.

## 2. Dot pre-tuning

Next, rough tuneup of the quantum dots is done via dc transport. We first isolate the dots from the wire by setting TG1 and TG2 below threshold. Transport is measured from Ohmic contact S1 to S2 with each dot formed by setting the adjacent cutter gates (i.e. SC or QC gate) to the tunneling regime and dot plungers and the remaining cutter gates in the current path to accumulation. A map of Coulomb diamonds as shown in Fig. 10 is used to verify successful tune-up. These maps can also be used to extract the lever arms and bare charging energies of the quantum dots as well as the level spacing. We extract charging energies of  $180 \mu\text{eV}$ ,  $60 \mu\text{eV}$ , and  $130 \mu\text{eV}$  for dot 1, dot 2, and dot 3, respectively. From Fig. 10a we estimate the level spacing of the left quantum dot  $\approx 100 \mu\text{eV}$ . Extrapolating to the  $\approx 5$  times larger dot 2 (see Fig. 1b) yields a level spacing of  $\approx 20 \mu\text{eV}$  which indeed significantly exceeds the temperature as assumed in our theoretical modeling.

Finally, the conductance is measured while sweeping rf drive power and  $V_{\text{QD}2}$  to observe broadening of the Coulomb blockade peaks and extract the lever arm used to convert rf drive power to voltage reaching the device.

We subsequently form a fully isolated triple quantum dot dot 1-dot 2-dot 3 by setting SC1 and SC2 below their threshold voltages while also leaving TG1 and TG2 below threshold. The dot plungers are left at the optimal value found in the single dot tune-up steps. First, a double quantum dot (DQD) is formed by setting QC2 below threshold. The rf response of dot 2 is monitored while sweeping the voltages  $V_{\text{QC}1}$  and  $V_{\text{QD}1}$ . The inter-dot quantum capacitance will give rise to a measurable rf response in a narrow window of QC1 voltage. Below this range the rf response is suppressed as the tunnel coupling drops below the temperature. Above this range, the magnitude of the quantum capacitance is suppressed by the large anti-crossing (and subsequently small curvature) of the DQD ground state. Once this optimal range in QC1 is identified, QC1 is set below threshold and the same procedure is repeated for QC2. With the optimal ranges of the two QC gates identified, a triple dot is formed in this isolated configuration by setting both QC gates to their optimal values. A triple dot charge stability diagram like the one shown in Fig. 10d is used to verify successful tuneup of the triple dot.

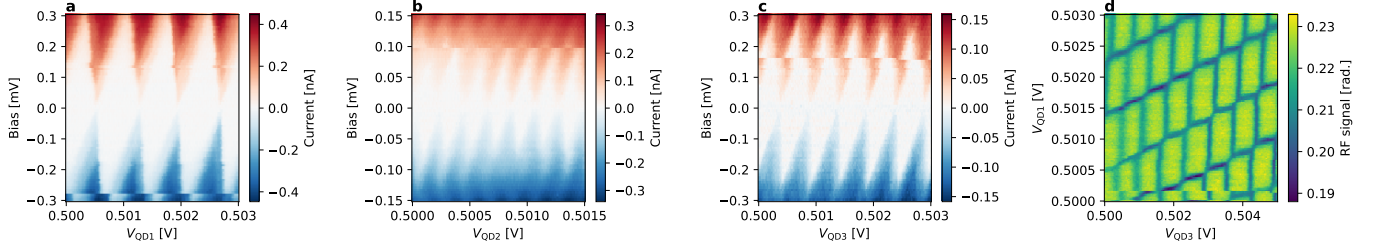


FIG. 10. Representative dot tune-up data. (a-c) Transport measurements of the respective single quantum dots when fully isolated from the nanowire (TG1 and TG2 set below their respective threshold voltages). (d) Dispersive gate sensing measurement of the charge stability diagram of the fully isolated triple-dot. TG1, TG2, SC1, and SC2 are all set below their respective threshold voltages. In this regime, the charging energies that have been extracted are as follows  $E_{C1} = 180\mu\text{eV}$ ,  $E_{C2} = 60\mu\text{eV}$ , and  $E_{C3} = 130\mu\text{eV}$ .

### 3. Topological Gap Protocol

With the optimal voltages for the dots identified, we now proceed with running the TGP. SC1 and SC2 are set back to accumulation while TG1 and TG2 are set to the tunneling regime to enable transport measurements on the wire again. The dot plungers are unchanged from the preceding step, and QC1 and QC2 are set below their threshold voltages to isolate S1 from S2. With the auxiliary gates configured in this manner, stages 1 and 2 of the TGP are run as described in Ref. 48.

### 4. Tuning the TQDI loop

After completion of a successful TGP, we select an in-plane magnetic field and WP1 voltage range with both sizeable transport gap and ZBP's at both ends of the wire. With this field and WP1 voltage selected, TG1 and TG2 are varied to achieve a strong coupling to the ZBP's. Once this coupling is established, SC1 and SC2 are set below threshold and all remaining measurements are done with dispersive gate sensing. In order to establish a loop configuration, we set QC1 and QC2 back to their optimal values found in the earlier triple dot tuning step. QD-MZM coupling and interferometry measurements are then performed as described in the main text.

#### Appendix D: Expected rf signal in Parity Readout and QD-MZM measurement configurations

We now turn to a simulation of a simple few-level model for the Majorana wire and the three quantum dots. By including effects of non-zero temperature, decoherence, finite drive and low-frequency charge noise as well as incorporating details about how the experimental data is taken, we will find remarkable agreement with the measured data.

The starting point is the model of Appendix B 1, including the two Majorana zero modes  $\gamma_{1,2}$  with splitting energy  $E_M$  and three quantum dots (dots 1 through 3),

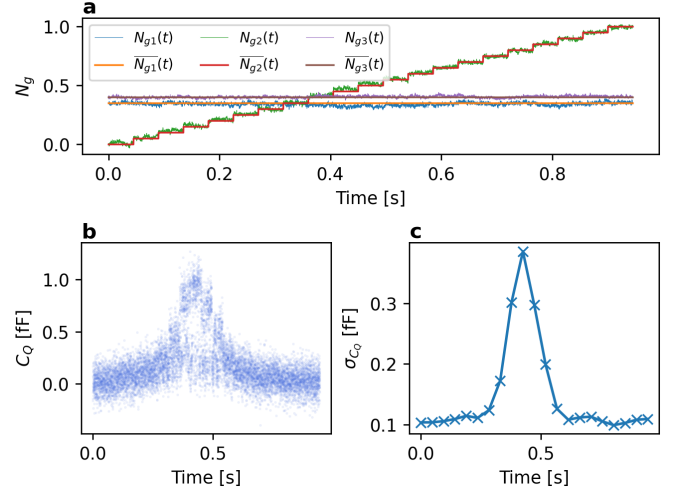


FIG. 11. Illustration of simulations of parity readout maps. The example shown here corresponds to a cut at fixed flux  $\Phi = 0.5h/2e$ . (a): Evolution of the gate voltages  $N_g(t)$ , where  $\bar{N}_g(t)$  indicates the intended evolution for each gate, including the stepping of the voltage on QD2 by 0.01 every 45 ms and keeping dot 1 fixed at  $N_{g1} = 0.35$  and dot 3 at  $N_{g3} = 0.4$ .  $N_g(t)$  indicates the noisy trajectory obtained after including the effects of low-frequency charge noise. (b):  $C_Q(t)$  obtained at each point in the time trajectory. (c): Standard deviation of the timetraces at each  $N_{g2}$ . This is the quantity that is compared between simulation and experiment.

tuned via gate charges  $N_{g1}$  through  $N_{g3}$ . The charging energies in the isolated QD regime are given in Fig. 10. When the interferometer loop is formed, the charging energies are renormalized down due to quantum charge fluctuations involving virtual transitions to states of higher energy (outside the low-energy subspace defined in (B5)). To estimate this effect, one can consider a model including an additional level in dot 2 (quantum dot with the smallest level spacing) and obtain a low-energy model using a Schrieffer-Wolff transformation, similarly to the derivation of Appendix B 2. By expanding the derived effective model near the charge degeneracy, one can estimate the renormalization of model parameters due to virtual transitions to excited states.

Using  $|t_{12}| = |t_{23}| = 12\mu\text{eV}$  and extracted bare charging energies, one finds the renormalized charging energies to be approximately given  $\tilde{E}_{C1} \approx 140\mu\text{eV}$ ,  $\tilde{E}_{C2} \approx 45\mu\text{eV}$ , and  $\tilde{E}_{C3} \approx 100\mu\text{eV}$ , respectively. The simulations presented in the main body of the paper employ these renormalized charging energies.

We treat the evolution of this system in the ULE formalism of Appendix B 4, where the coupling to the environment is included through charge noise on each of the three quantum dots. The corresponding Lindblad operators are obtained within the ULE framework for system operators  $X_i = n_{\text{QD},i}$ ,  $i = 1, 2, 3$ , where  $n_{\text{QD},i}$  is the number operator for each of the three dots, and the spectral function is given by

$$S_g(\omega) = \frac{\gamma}{1 + \exp(-\hbar\omega/k_B T)} \quad (\text{D1})$$

with  $\gamma = 1\text{GHz}$  and  $T = 75\text{mK}$ . This choice of  $\gamma$  is motivated by matching the typical strength of  $1/\omega$  charge noise in quantum dot experiments evaluated at  $\omega \approx 5\mu\text{eV}$ , which is the relevant energy scale for these simulations. It is worth noting that the precise value chosen here has only very small effect on the real part of  $C_Q$ , as it mainly controls the rate of thermalization. We ignore noise on the couplings, which is expected to be much weaker than charge noise on the quantum dot detunings. We introduce a drive on  $N_{g2}$ , i.e. we replace  $N_{g2} \rightarrow N_{g2} + (A_{\text{rf}}/2E_{C2}) \cos(\omega t)$ , where we choose  $A_{\text{rf}} = 5\mu\text{eV}$  (note that  $A_{\text{rf}} = \alpha V_{\text{rf}}$ , where  $\alpha \approx 0.5$  is the lever arm) and  $E_{C2}$  corresponds to the charging energy of dot 2. This thus defines a simulated response  $C_Q(N_{g1}, N_{g2}, N_{g3}, \Phi, Z)$ , where  $\Phi$  is the flux enclosed in the loop and  $Z$  is the overall parity of the system.

The final step is to include low-frequency charge noise, readout noise, parity flips, and the way the experimental data is acquired. As an example, we can consider the parity readout maps as shown in, e.g., Fig. 2(a). These consist of timetraces of about 50ms duration at each point in the  $(N_{g2}, B_{\perp})$  plane, where  $N_{g2}$  constitutes the inner loop and  $B_{\perp}$  the outer loop. Measurements are taken at approximately 100 points in  $N_{g2}$  (typically spanning 5 charge transitions) and 70 points in  $B_{\perp}$ ; the total time for a single measurement panel is thus approximately 320s. To generate this behavior, we generate time traces of all parameters of the system. For each gate voltage, we generate a trajectory  $N_{g,i}(t) = \overline{N_{g,i}}(t) + \delta N_{g,i}(t)$ , where  $\overline{N_{g,i}}(t)$  is a function describing the ideal parameter evolution and  $\delta N_{g,i}(t)$  is a noise trajectory whose power spectral density is given by  $\alpha_C^2/\omega$  (see Fig. 11(a)). Here, we choose  $\alpha_C = 0.00675$ , again motivated by the typical amount of charge noise observed in comparable QD systems. The tuning parameter evolution  $\overline{N_{g,i}}(t)$  is a constant in the case of the side dots, whereas for dot 2 it is a function that increases from 0 to 1 in 20 steps over  $20 \times 50\text{ms}$ . For the parity  $Z(t)$ , we generate a telegraph noise trajectory with a symmetric transition rate of  $\Gamma_{\text{qpp}} = (1\text{ms})^{-1}$ . Finally, the flux  $\Phi(t)$  is stepped from 0 to  $4h/2e$  in 70 increments. The readout noise is added

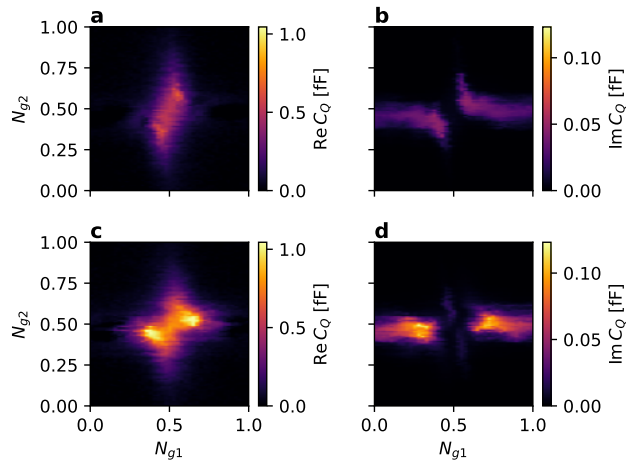


FIG. 12. Simulations of the configuration used for extracting the QD-MZM couplings, where one of the side dots (here dot 3) is maximally detuned while the gate voltages on the other two dots are being varied. The couplings used here are  $t_{12} = t_{23} = 12\mu\text{eV}$ , and  $t_{m2} = 6\mu\text{eV}$  in the top panels and  $t_{m1} = 6\mu\text{eV}$  in the bottom panels; left and right panels show the real and imaginary part of the  $C_Q$  response, respectively. Unlike the parity measurement, the length of time traces is chosen to be 10ms.

as Gaussian noise with standard deviation  $\sigma_{C_Q}$ , where we choose  $\sigma_{C_Q} = 0.105\text{fF}$  in line with the experimental observation in Fig. 9. Taken together, this allows us to define  $C_Q(t) = C_Q(N_{g1}(t), N_{g2}(t), N_{g3}(t), \Phi(t), Z(t))$  in a data format that exactly reproduces that of the experimental data, see Fig. 11(b) and (c).

### 1. QD-MZM maps

The same general approach can be used to simulate the response in the QD-MZM configuration introduced in Appendix C, where one of the side quantum dots is completely detuned so that the coupling between the dot 2 and the topological wire is dominated by the other QD-MZM couplings. Fig. 12 shows the  $C_Q$  response of dot 2 simulated for this configuration in the limit of very small and very large coupling between  $\gamma_1$  and dot 1, while dot 3 is fully detuned. One can see that both the shape and magnitude of the  $C_Q$  response depend significantly on  $t_{m1}$ . As discussed in the main text, the parameters of the model can be extracted using the quantitative features of these maps.

### Appendix E: Measurement of non-equilibrium quasiparticle density in a Cooper pair box device

To gain a deeper understanding of the quasiparticle poisoning phenomenon in our devices and to extract the non-equilibrium quasiparticle density we have designed

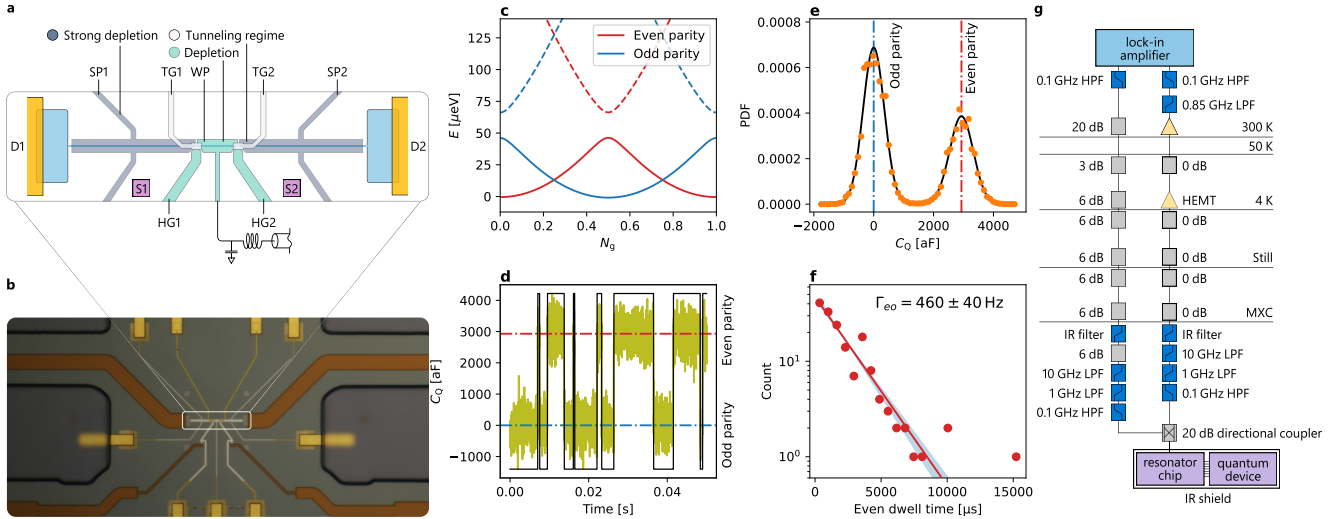


FIG. 13. Cooper pair box (CPB) quasiparticle poisoning measurement. (a) Schematic of the CPB device, with the resonator connected to the CPB plunger gate. (b) An optical image of an equivalent device. (c) Energy levels of the island, with even(odd) parity branches marked in red(blue), and excited states (dashed lines). (d) Section of a representative time trace showing the extracted quantum capacitance shift. Quasiparticle poisoning events are clearly visible, with the extracted parity marked in black. (e) Distribution of  $C_Q$  values across a time trace. The SNR of this measurement is 3.8. (f) Distribution of even dwell times and an exponential fit to the data, showing a poisoning rate of 460(40) Hz.  $1\sigma$  confidence interval is marked in blue. (g) Schematic of the readout chain connected to the resonator.

Param.	Description	Value
$f_0$	Resonator frequency	776.5 MHz
$\kappa_{\text{ext}}/2\pi$	Resonator readout coupling	14.8 MHz
$\kappa_{\text{int}}/2\pi$	Resonator internal loss	<1.5 MHz
$\Delta_0$	Parent superconducting gap	275 $\mu\text{eV}$
$E_C$	Charging energy	225 $\mu\text{eV}$
$E_J$	Josephson energy	20 $\mu\text{eV}$
$\alpha$	Gate lever arm	0.8
$g$	NS Dimensionless conductance	0.3
$\nu_{\text{Al}}$	Normal DOS of aluminum	$3 \times 10^4 \mu\text{eV}^{-1} \mu\text{m}^{-3}$

TABLE II. Measured device parameters for the Cooper pair box device.

and fabricated an auxiliary device. This device consists of a Cooper pair box (CPB), which is coupled to superconducting leads via two gate-controlled Josephson junctions, as illustrated in Fig. 13a. The device is fabricated on a comparable InAs/InAlAs heterostructure, maintaining the same wire width to ensure that the cross-section of the device matches that of the TQDI device. The plunger gate for the CPB is coupled to a resonator similar to that of the TQDI device, the parameters of which are listed in Table II. This setup allows for the direct measurement of the island's parity by observing the dispersive shift in the time domain, as outlined in Appendix A 4 and discussed in Ref. [74].

During the measurement, the device is operated in the Cooper pair box regime where one of the Josephson junctions is closed. The measured parameters of the device

are summarized in Table II. The device is then tuned to an odd offset charge which we refer to as  $N_g = 1$  which leads to a degeneracy of the  $N = 0$  and  $N = 2$  state of the Cooper pair box. The finite Josephson energy then leads to an avoided crossing which gives rise to a quantum capacitance

$$C_Q^{\text{CPB}} = \frac{8e^2\alpha^2 E_J^2 \tanh\left(\sqrt{(2\alpha e V_g)^2 + 4E_J^2}/2k_B T\right)}{[(2\alpha e V_g)^2 + 4E_J^2]^{3/2}}. \quad (\text{E1})$$

Here  $V_g$  and  $\alpha$  are the plunger gate voltage and corresponding lever arm of the Cooper pair box, respectively. When the device is in the odd state due to a quasiparticle poisoning event, the charge states differing by a Cooper pair are no longer resonant and the quantum capacitance vanishes. The parity-dependence of the quantum capacitance then leads to a random telegraph signal, from which, by continuously observing the capacitive response, we can directly extract the poisoning rate. The sample enclosure and dc filtering are chosen to be equivalent to the TQDI device, however the readout circuit utilizes a Caltech CITLF3 amplifier and places the IR filters before the coupler, at the mixing chamber stage. A schematic of the circuit is shown in Fig. 13g. We expect that the differences between the readout circuits are negligible, or will degrade performance relative to the configuration in the main experiment, meaning the extracted number here will act as an upper bound on the quasiparticle density. The measurement and subsequent extraction of parity closely follows the procedure detailed in Ref. [74], with a filter bandwidth of 100 kHz,

much shorter than the extracted time constant of quasiparticle poisoning. A subsection of a representative RTS trace, with the readout signal converted to units of  $C_Q$  following the method detailed in Appendix A 5, is shown in Fig. 13d. We assign the even/odd parity states based on thresholding the  $C_Q$  signal. Whenever the signal exceeds the mean of the even parity we label it as even and keep that label until it drops below the mean of odd parity state. This method is also used to label the data in Fig. 2e and works well in suppressing state mislabeling due to finite SNR.<sup>2</sup> Finally, we extract  $\Gamma_{\text{EO}} = 460(40)$  Hz by fitting the even-state dwell-time distribution to an exponential distribution as shown in Fig. 13f.

The extracted even-to-odd switching rate  $\Gamma_{\text{EO}}$  can be

connected [74] to the quasiparticle density via

$$\Gamma_{\text{EO}} = \frac{g}{4\pi} \frac{n_{\text{qp}}^{\text{CPB}}}{\nu_{\text{Al}}} \sqrt{\frac{\delta E}{2\Delta_0}}, \quad (\text{E2})$$

where  $g$  is the normal state dimensionless conductance of the Josephson junction,  $\delta E = E_C - E_J/2$ ,  $\Delta_0$  is the (parent) superconducting gap, and  $\nu_{\text{Al}}$  is the Al density of states at the Fermi level. We extract the charging energy  $E_C$  and lever arm  $\alpha$  from Coulomb diamonds (not shown). We can then use Eq. (E1) to fit the width of the peak in  $C_Q^{\text{CPB}}$  when changing the gate voltage of the Cooper pair box to determine  $E_J$ , which yields  $g = 4E_J/\Delta_0$ . With these parameters we find using Eq. (E2)  $n_{\text{qp}}^{\text{CPB}} \approx 0.6 \mu\text{m}^{-3}$ , close to the measured value of the TQDI device of  $n_{\text{qp}} \approx 1 \mu\text{m}^{-3}$ . For the TQDI device, this density would yield an expected QPP time of  $\tau_{\text{QPP}} \approx 3$  ms, close to the measured value of 2 ms quoted in the main text.

- 
- [1] A. Y. Kitaev, Fault-tolerant quantum computation by anyons, *Ann. Phys.* **303**, 2 (2003), [quant-ph/9707021](#).
- [2] M. H. Freedman, *P/NP*, and the quantum field computer, *Proc. Natl. Acad. Sci. USA* **95**, 98 (1998).
- [3] C. Nayak, S. H. Simon, A. Stern, M. Freedman, and S. Das Sarma, Non-Abelian anyons and topological quantum computation, *Rev. Mod. Phys.* **80**, 1083 (2008), [arXiv:0707.1889](#).
- [4] P. Bonderson, M. Freedman, and C. Nayak, Measurement-only topological quantum computation, *Phys. Rev. Lett.* **101**, 010501 (2008), [arXiv:0802.0279](#).
- [5] P. Bonderson, M. Freedman, and C. Nayak, Measurement-only topological quantum computation via anyonic interferometry, *Ann. Phys.* **324**, 787 (2009), [arXiv:0808.1933](#).
- [6] T. Karzig, C. Knapp, R. M. Lutchyn, P. Bonderson, M. B. Hastings, C. Nayak, J. Alicea, K. Flensberg, S. Plugge, Y. Oreg, C. M. Marcus, and M. H. Freedman, Scalable designs for quasiparticle-poisoning-protected topological quantum computation with Majorana zero modes, *Phys. Rev. B* **95**, 235305 (2017).
- [7] C. Knapp, M. Beverland, D. I. Pikulin, and T. Karzig, Modeling noise and error correction for Majorana-based quantum computing, *Quantum* **2**, 88 (2018).
- [8] M. B. Hastings and J. Haah, Dynamically generated logical qubits, *Quantum* **5**, 564 (2021).
- [9] A. Paetznick, C. Knapp, N. Delfosse, B. Bauer, J. Haah, M. B. Hastings, and M. P. da Silva, Performance of planar Floquet codes with Majorana-based qubits, *PRX Quantum* **4**, 010310 (2023).
- [10] L. Grans-Samuelsson, R. V. Mishmash, D. Aasen, C. Knapp, B. Bauer, B. Lackey, M. P. da Silva, and P. Bonderson, Improved pairwise measurement-based surface code (2023), [arXiv:2310.12981](#).
- [11] A. G. Fowler, M. Mariantoni, J. M. Martinis, and A. N. Cleland, Surface codes: Towards practical large-scale quantum computation, *Phys. Rev. A* **86**, 032324 (2012).
- [12] J. Preskill, Quantum Computing in the NISQ era and beyond, *Quantum* **2**, 79 (2018).
- [13] C. Gidney and M. Ekerå, How to factor 2048 bit RSA integers in 8 hours using 20 million noisy qubits, *Quantum* **5**, 433 (2021).
- [14] M. E. Beverland, P. Murali, M. Troyer, K. M. Svore, T. Hoefler, V. Kliuchnikov, G. H. Low, M. Soeken, A. Sundaram, and A. Vassallo, Assessing requirements to scale to practical quantum advantage (2022), [2211.07629](#).
- [15] A. Y. Kitaev, Unpaired Majorana fermions in quantum wires, *Phys.-Usp.* **44**, 31 (2001), [arXiv:cond-mat/0010440](#).
- [16] R. M. Lutchyn, J. D. Sau, and S. Das Sarma, Majorana Fermions and a topological phase transition in semiconductor-superconductor heterostructures, *Phys. Rev. Lett.* **105**, 077001 (2010), [arXiv:1002.4033](#).
- [17] Y. Oreg, G. Refael, and F. von Oppen, Helical liquids and Majorana bound states in quantum wires, *Phys. Rev. Lett.* **105**, 177002 (2010), [arXiv:1003.1145](#).
- [18] R. M. Lutchyn, E. P. A. M. Bakkers, L. P. Kouwenhoven, P. Krogstrup, C. M. Marcus, and Y. Oreg, Majorana zero modes in superconductor-semiconductor heterostructures, *Nat. Rev. Mater.* **3**, 52 (2018).
- [19] J. Alicea, New directions in the pursuit of Majorana fermions in solid state systems, *Rep. Prog. Phys.* **75**, 076501 (2012), [arXiv:1202.1293](#).
- [20] S. D. Sarma, M. Freedman, and C. Nayak, Majorana zero modes and topological quantum computation, *npj Quantum Inf.* **1**, 15001 (2015).
- [21] D. Aasen, M. Hell, R. V. Mishmash, A. Higginbotham, J. Danon, M. Leijnse, T. S. Jespersen, J. A. Folk, C. M. Marcus, K. Flensberg, and J. Alicea, Milestones toward Majorana-based quantum computing, *Phys. Rev. X* **6**,

<sup>2</sup> In addition, for the labeling of the data used in Fig. 2e, one needs to take into account that there the assignment of high/low values of  $C_Q$  for the even/odd parities switches as a function of flux with an  $h/e$  periodicity.

- 031016 (2016), arXiv:1511.05153.
- [22] J. D. Sau, D. J. Clarke, and S. Tewari, Controlling non-Abelian statistics of Majorana fermions in semiconductor nanowires, *Phys. Rev. B* **84**, 094505 (2011), arXiv:1012.0561.
- [23] B. van Heck, A. R. Akhmerov, F. Hassler, M. Burrello, and C. W. J. Beenakker, Coulomb-assisted braiding of Majorana fermions in a Josephson junction array, *New J. Phys.* **14**, 035019 (2012), arXiv:1111.6001.
- [24] T. Hyart, B. van Heck, I. C. Fulga, M. Burrello, A. R. Akhmerov, and C. W. J. Beenakker, Flux-controlled quantum computation with Majorana fermions, *Phys. Rev. B* **88**, 035121 (2013), arXiv:1303.4379.
- [25] L. Fu and C. L. Kane, Josephson current and noise at a superconductor/quantum-spin-Hall-insulator/superconductor junction, *Phys. Rev. B* **79**, 161408(R) (2009).
- [26] A. R. Akhmerov, J. Nilsson, and C. W. J. Beenakker, Electrically detected interferometry of Majorana fermions in a topological insulator, *Phys. Rev. Lett.* **102**, 216404 (2009), arXiv:0903.2196.
- [27] L. Fu and C. L. Kane, Probing neutral Majorana fermion edge modes with charge transport, *Phys. Rev. Lett.* **102**, 216403 (2009).
- [28] F. Hassler, A. R. Akhmerov, C.-Y. Hou, and C. W. J. Beenakker, Anyonic interferometry without anyons: how a flux qubit can read out a topological qubit, *New J. Phys.* **12**, 125002 (2010), arXiv:1005.3423.
- [29] L. Fu, Electron teleportation via Majorana bound states in a mesoscopic superconductor, *Phys. Rev. Lett.* **104**, 056402 (2010), arXiv:0909.5172.
- [30] B. van Heck, F. Hassler, A. R. Akhmerov, and C. W. J. Beenakker, Coulomb stability of the  $4\pi$ -periodic Josephson effect of Majorana fermions, *Phys. Rev. B* **84**, 180502 (2011).
- [31] M. Cheng and R. Lutchyn, Fractional Josephson effect in number-conserving systems, *Phys. Rev. B* **92**, 134516 (2015).
- [32] M. Hell, K. Flensberg, and M. Leijnse, Distinguishing Majorana bound states from localized Andreev bound states by interferometry, *Phys. Rev. B* **97**, 161401 (2018).
- [33] C.-K. Chiu, J. D. Sau, and S. Das Sarma, Conductance interference in a superconducting Coulomb blocked Majorana ring, *Phys. Rev. B* **97**, 035310 (2018).
- [34] C. Drukier, H.-G. Zirnstein, B. Rosenow, A. Stern, and Y. Oreg, Evolution of the transmission phase through a Coulomb-blockaded Majorana wire, *Phys. Rev. B* **98**, 161401 (2018).
- [35] L. Fidkowski, R. M. Lutchyn, C. Nayak, and M. P. A. Fisher, Majorana zero modes in one-dimensional quantum wires without long-ranged superconducting order, *Phys. Rev. B* **84**, 195436 (2011), arXiv:1106.2598.
- [36] S. Plugge, L. A. Landau, E. Sela, A. Altland, K. Flensberg, and R. Egger, Roadmap to Majorana surface codes, *Phys. Rev. B* **94**, 174514 (2016).
- [37] S. Plugge, A. Rasmussen, R. Egger, and K. Flensberg, Majorana box qubits, *New J. Phys.* **19**, 012001 (2017).
- [38] S. Vijay, T. H. Hsieh, and L. Fu, Majorana fermion surface code for universal quantum computation, *Phys. Rev. X* **5**, 041038 (2015), arXiv:1504.01724.
- [39] S. Vijay and L. Fu, Physical implementation of a Majorana fermion surface code for fault-tolerant quantum computation, *Phys. Scr.* **T168**, 014002 (2016), arXiv:1509.08134.
- [40] S. Vijay and L. Fu, Teleportation-based quantum information processing with Majorana zero modes, *Phys. Rev. B* **94**, 235446 (2016), arXiv:1609.00950.
- [41] A. M. Whiticar, A. Fornieri, E. C. T. O'Farrell, A. C. C. Drachmann, T. Wang, C. Thomas, S. Gronin, R. Kallagher, G. C. Gardner, M. J. Manfra, C. M. Marcus, and F. Nichele, Coherent transport through a Majorana island in an Aharonov–Bohm interferometer, *Nat. Commun.* **11**, 3212 (2020).
- [42] C. Janvier, L. Tosi, L. Bretheau, Ç. Ö. Girit, M. Stern, P. Bertet, P. Joyes, D. Vion, D. Esteve, M. F. Goffman, H. Pothier, and C. Urbina, Coherent manipulation of Andreev states in superconducting atomic contacts, *Science* **349**, 1199 (2015).
- [43] M. Hays, G. de Lange, K. Serniak, D. J. van Woerkom, D. Bouman, P. Krogstrup, J. Nygård, A. Geresdi, and M. H. Devoret, Direct microwave measurement of Andreev-bound-state dynamics in a semiconductor-nanowire Josephson junction, *Phys. Rev. Lett.* **121**, 047001 (2018).
- [44] M. Hays, V. Fatemi, D. Bouman, J. Cerrillo, S. Diamond, K. Serniak, T. Connolly, P. Krogstrup, J. Nygård, A. L. Yeyati, A. Geresdi, and M. H. Devoret, Coherent manipulation of an Andreev spin qubit, *Science* **373**, 430 (2021).
- [45] J. J. Wesdorp, L. Grünhaupt, A. Vaartjes, M. Pita-Vidal, A. Bargerbos, L. J. Splitthoff, P. Krogstrup, B. van Heck, and G. de Lange, Dynamical polarization of the fermion parity in a nanowire Josephson junction, *Phys. Rev. Lett.* **131**, 117001 (2023), arXiv:2112.01936.
- [46] M. Aghaee *et al.* (Microsoft Quantum), In preparation.
- [47] D. I. Pikulin, B. van Heck, T. Karzig, E. A. Martinez, B. Nijholt, T. Laeven, G. W. Winkler, J. D. Watson, S. Heedt, M. Temurhan, V. Svidenko, R. M. Lutchyn, M. Thomas, G. de Lange, L. Casparis, and C. Nayak, Protocol to identify a topological superconducting phase in a three-terminal device (2021), arXiv:2103.12217.
- [48] M. Aghaee *et al.* (Microsoft Quantum), InAs-Al hybrid devices passing the topological gap protocol, *Phys. Rev. B* **107**, 245423 (2023).
- [49] H. J. Suominen, M. Kjaergaard, A. R. Hamilton, J. Shabani, C. J. Palmström, C. M. Marcus, and F. Nichele, Zero-energy modes from coalescing Andreev states in a two-dimensional semiconductor-superconductor hybrid platform, *Phys. Rev. Lett.* **119**, 176805 (2017).
- [50] F. Nichele, A. C. C. Drachmann, A. M. Whiticar, E. C. T. O'Farrell, H. J. Suominen, A. Fornieri, T. Wang, G. C. Gardner, C. Thomas, A. T. Hatke, P. Krogstrup, M. J. Manfra, K. Flensberg, and C. M. Marcus, Scaling of Majorana zero-bias conductance peaks, *Phys. Rev. Lett.* **119**, 136803 (2017).
- [51] A. Pöschl, A. Danilenko, D. Sabonis, K. Kristjūhan, T. Lindemann, C. Thomas, M. J. Manfra, and C. M. Marcus, Nonlocal conductance spectroscopy of Andreev bound states in gate-defined InAs/Al nanowires, *Phys. Rev. B* **106**, L241301 (2022), arXiv:2204.02430.
- [52] G. C. Ménard, F. K. Malinowski, D. Puglia, D. I. Pikulin, T. Karzig, B. Bauer, P. Krogstrup, and C. M. Marcus, Suppressing quasiparticle poisoning with a voltage-controlled filter, *Phys. Rev. B* **100**, 165307 (2019).
- [53] J. I. Colless, A. C. Mahoney, J. M. Hornibrook, A. C.

- Doherty, H. Lu, A. C. Gossard, and D. J. Reilly, Dispersive readout of a few-electron double quantum dot with fast rf gate sensors, *Phys. Rev. Lett.* **110**, 046805 (2013), [arXiv:1210.4645](https://arxiv.org/abs/1210.4645).
- [54] J. M. Hornibrook, J. I. Colless, A. C. Mahoney, X. G. Croot, S. Blanvillain, H. Lu, A. C. Gossard, and D. J. Reilly, Frequency multiplexing for readout of spin qubits, *Appl. Phys. Lett.* **104**, 10.1063/1.4868107 (2014).
- [55] A. P. Higginbotham, T. W. Larsen, J. Yao, H. Yan, C. M. Lieber, C. M. Marcus, and F. Kueemeth, Hole spin coherence in a Ge/Si heterostructure nanowire, *Nano Letters* **14**, 3582–3586 (2014).
- [56] I. Ahmed, J. A. Haigh, S. Schaal, S. Barraud, Y. Zhu, C.-m. Lee, M. Amado, J. W. A. Robinson, A. Rossi, J. J. L. Morton, and M. F. Gonzalez-Zalba, Radio-frequency capacitive gate-based sensing, *Phys. Rev. Appl.* **10**, 014018 (2018).
- [57] D. de Jong, J. van Veen, L. Binci, A. Singh, P. Krogstrup, L. P. Kouwenhoven, W. Pfaff, and J. D. Watson, Rapid detection of coherent tunneling in an InAs nanowire quantum dot through dispersive gate sensing, *Phys. Rev. Appl.* **11**, 044061 (2019).
- [58] J. van Veen, D. de Jong, L. Han, C. Prosko, P. Krogstrup, J. D. Watson, L. P. Kouwenhoven, and W. Pfaff, Revealing charge-tunneling processes between a quantum dot and a superconducting island through gate sensing, *Phys. Rev. B* **100**, 174508 (2019).
- [59] D. Sabonis, E. C. T. O’Farrell, D. Razmadze, D. M. T. van Zanten, J. Suter, P. Krogstrup, and C. M. Marcus, Dispersive sensing in hybrid InAs/Al nanowires, *Appl. Phys. Lett.* **115**, 102601 (2019).
- [60] S. Schaal, I. Ahmed, J. A. Haigh, L. Hutin, B. Bertrand, S. Barraud, M. Vinet, C.-M. Lee, N. Stelmashenko, J. W. A. Robinson, J. Y. Qiu, S. Hacoheh-Gourgy, I. Siddiqi, M. F. Gonzalez-Zalba, and J. J. L. Morton, Fast gate-based readout of silicon quantum dots using Josephson parametric amplification, *Phys. Rev. Lett.* **124**, 067701 (2020).
- [61] F. K. Malinowski, L. Han, D. De Jong, J.-Y. Wang, C. G. Prosko, G. Badawy, S. Gazibegovic, Y. Liu, P. Krogstrup, E. P. Bakkers, *et al.*, Radio-frequency *c-v* measurements with subattofarad sensitivity, *Phys. Rev. Appl.* **18**, 024032 (2022).
- [62] C. Macklin, K. O’Brien, D. Hover, M. Schwartz, V. Bolkhovskiy, X. Zhang, W. Oliver, and I. Siddiqi, A near-quantum-limited Josephson traveling-wave parametric amplifier, *Science* **350**, 307 (2015).
- [63] R. Barends, J. Wenner, M. Lenander, Y. Chen, R. C. Bialczak, J. Kelly, E. Lucero, P. O’Malley, M. Mariantoni, D. Sank, H. Wang, T. C. White, Y. Yin, J. Zhao, A. N. Cleland, J. M. Martinis, and J. J. A. Baselmans, Minimizing quasiparticle generation from stray infrared light in superconducting quantum circuits, *Appl. Phys. Lett.* **99**, 113507 (2011).
- [64] S. Diamond, V. Fatemi, M. Hays, H. Nho, P. D. Kurilovich, T. Connolly, V. R. Joshi, K. Serniak, L. Frunzio, L. I. Glazman, and M. H. Devoret, Distinguishing parity-switching mechanisms in a superconducting qubit, *PRX Quantum* **3**, 040304 (2022).
- [65] D. J. Clarke, Experimentally accessible topological quality factor for wires with zero energy modes, *Physical Review B* **96**, 10.1103/physrevb.96.201109 (2017).
- [66] E. Prada, R. Aguado, and P. San-Jose, Measuring majorana nonlocality and spin structure with a quantum dot, *Physical Review B* **96**, 10.1103/physrevb.96.085418 (2017).
- [67] M. T. Deng, S. Vaitiekenas, E. B. Hansen, J. Danon, M. Leijnse, K. Flensberg, J. Nygård, P. Krogstrup, and C. M. Marcus, Majorana bound state in a coupled quantum-dot hybrid-nanowire system, *Science* **354**, 1557 (2016).
- [68] I. Aleiner, P. Brouwer, and L. Glazman, Quantum effects in Coulomb blockade, *Phys. Rep.* **358**, 309–440 (2002).
- [69] C. G. Prosko, I. Kulesh, M. Chan, L. Han, D. Xiao, C. Thomas, M. J. Manfra, S. Goswami, and F. K. Malinowski, Flux-tunable hybridization in a double quantum dot interferometer, [arXiv:2303.04144](https://arxiv.org/abs/2303.04144) (2023).
- [70] J. Aumentado, M. W. Keller, J. M. Martinis, and M. H. Devoret, Nonequilibrium quasiparticles and  $2e$  periodicity in single-Cooper-pair transistors, *Phys. Rev. Lett.* **92**, 066802 (2004).
- [71] O. Naaman and J. Aumentado, Time-domain measurements of quasiparticle tunneling rates in a single-Cooper-pair transistor, *Phys. Rev. B* **73**, 172504 (2006).
- [72] R. M. Lutchyn, L. I. Glazman, and A. I. Larkin, Kinetics of the superconducting charge qubit in the presence of a quasiparticle, *Phys. Rev. B* **74**, 10.1103/physrevb.74.064515 (2006).
- [73] A. J. Ferguson, N. A. Court, F. E. Hudson, and R. G. Clark, Microsecond resolution of quasiparticle tunneling in the single-Cooper-pair transistor, *Phys. Rev. Lett.* **97**, 106603 (2006).
- [74] M. D. Shaw, R. M. Lutchyn, P. Delsing, and P. M. Echternach, Kinetics of nonequilibrium quasiparticle tunneling in superconducting charge qubits, *Phys. Rev. B* **78**, 024503 (2008).
- [75] F. Persson, C. M. Wilson, M. Sandberg, and P. Delsing, Fast readout of a single Cooper-pair box using its quantum capacitance, *Phys. Rev. B* **82**, 134533 (2010).
- [76] D. Ristè, C. Bultink, M. J. Tiggelman, R. N. Schouten, K. W. Lehnert, and L. DiCarlo, Millisecond charge-parity fluctuations and induced decoherence in a superconducting transmon qubit, *Nat. Commun.* **4**, 1913 (2013).
- [77] K. Serniak, S. Diamond, M. Hays, V. Fatemi, S. Shankar, L. Frunzio, R. J. Schoelkopf, and M. H. Devoret, Direct dispersive monitoring of charge parity in offset-charge-sensitive transmons, *Phys. Rev. Appl.* **12**, 014052 (2019), [arXiv:1903.00113](https://arxiv.org/abs/1903.00113).
- [78] W. Uilhoorn, J. G. Kroll, A. Bargerbos, S. D. Nabi, C.-K. Yang, P. Krogstrup, L. P. Kouwenhoven, A. Kou, and G. de Lange, Quasiparticle trapping by orbital effect in a hybrid superconducting-semiconducting circuit (2021), [arXiv:2105.11038](https://arxiv.org/abs/2105.11038).
- [79] E. T. Mannila, P. Samuelsson, S. Simbierowicz, J. T. Peltonen, V. Vesterinen, L. Grönberg, J. Hassel, V. F. Maisi, and J. P. Pekola, A superconductor free of quasiparticles for seconds, *Nat. Phys.* **18**, 145 (2022), [arXiv:2102.00484](https://arxiv.org/abs/2102.00484).
- [80] O. Erlandsson, D. Sabonis, A. Kringhøj, T. W. Larsen, P. Krogstrup, K. D. Petersson, and C. M. Marcus, Parity switching in a full-shell superconductor-semiconductor nanowire qubit, *Phys. Rev. B* **108**, L121406 (2023), [arXiv:2202.05974](https://arxiv.org/abs/2202.05974).
- [81] C. Knapp, T. Karzig, R. M. Lutchyn, and C. Nayak, Dephasing of Majorana-based qubits, *Phys. Rev. B* **97**,

- 125404 (2018).
- [82] T. Karzig, W. S. Cole, and D. I. Pikulin, Quasiparticle poisoning of Majorana qubits, *Phys. Rev. Lett.* **126**, 057702 (2021).
- [83] D. H. Cobden, A. Savchenko, M. Pepper, N. K. Patel, D. A. Ritchie, J. E. F. Frost, and G. A. C. Jones, Time-irreversible random telegraph signal due to current along a single hopping chain, *Phys. Rev. Lett.* **69**, 502 (1992).
- [84] M. Peters, J. Dijkhuis, and L. Molenkamp, Random telegraph signals and  $1/f$  noise in a silicon quantum dot, *J. Appl. Phys.* **86**, 1523 (1999).
- [85] M. Piore-Ladrière, J. H. Davies, A. R. Long, A. S. Sachrajda, L. Gaudreau, P. Zawadzki, J. Lapointe, J. Gupta, Z. Wasilewski, and S. Studenikin, Origin of switching noise in GaAs/Al<sub>x</sub>Ga<sub>1-x</sub>As lateral gated devices, *Phys. Rev. B* **72**, 115331 (2005).
- [86] C. Buizert, F. H. L. Koppens, M. Piore-Ladrière, H.-P. Tranitz, I. T. Vink, S. Tarucha, W. Wegscheider, and L. M. K. Vandersypen, *InSitu* reduction of charge noise in GaAs/Al<sub>x</sub>Ga<sub>1-x</sub>As Schottky-gated devices, *Phys. Rev. Lett.* **101**, 226603 (2008).
- [87] S. Das Sarma, J. Sau, and T. Stanescu, A Majorana smoking gun for the superconductor-semiconductor hybrid topological system (2012), [arXiv:1211.0539](https://arxiv.org/abs/1211.0539).
- [88] S. M. Albrecht, A. P. Higginbotham, M. Madsen, F. Kuemmeth, T. S. Jespersen, J. Nygård, P. Krogstrup, and C. M. Marcus, Exponential protection of zero modes in Majorana islands, *Nature (London)* **531**, 206 (2016), [arXiv:1603.03217](https://arxiv.org/abs/1603.03217).
- [89] S. Vaitiekėnas, G. W. Winkler, B. van Heck, T. Karzig, M.-T. Deng, K. Flensberg, L. I. Glazman, C. Nayak, P. Krogstrup, R. M. Lutchyn, and C. M. Marcus, Flux-induced topological superconductivity in full-shell nanowires, *Science* **367**, eaav3392 (2020).
- [90] J. Shabani, M. Kjaergaard, H. J. Suominen, Y. Kim, F. Nichele, K. Pakrouski, T. Stankevič, R. M. Lutchyn, P. Krogstrup, R. Feidenhans'l, S. Kraemer, C. Nayak, M. Troyer, C. M. Marcus, and C. J. Palmstrøm, Two-dimensional epitaxial superconductor-semiconductor heterostructures: A platform for topological superconducting networks, *Phys. Rev. B* **93**, 155402 (2016), [arXiv:1511.01127](https://arxiv.org/abs/1511.01127).
- [91] S. Schuwalow, N. B. M. Schröter, J. Gukelberger, C. Thomas, V. Strocov, J. Gamble, A. Chikina, M. Caputo, J. Krieger, G. C. Gardner, M. Troyer, G. Aeppli, M. J. Manfra, and P. Krogstrup, Band structure extraction at hybrid narrow-gap semiconductor-metal interfaces, *Adv. Sci.* **8**, 2003087 (2021).
- [92] F. K. Malinowski, R. Rupesh, L. Pavešić, Z. Guba, D. de Jong, L. Han, C. G. Prosko, M. Chan, Y. Liu, P. Krogstrup, *et al.*, Quantum capacitance of a superconducting subgap state in an electrostatically floating dot-island (2022), [arXiv:2210.01519](https://arxiv.org/abs/2210.01519).
- [93] S. Probst, F. B. Song, P. A. Bushev, A. V. Ustinov, and M. Weides, Efficient and robust analysis of complex scattering data under noise in microwave resonators, *Rev. Sci. Instrum.* **86**, 024706 (2015).
- [94] O. Motrunich, K. Damle, and D. A. Huse, Griffiths effects and quantum critical points in dirty superconductors without spin-rotation invariance: One-dimensional examples, *Phys. Rev. B* **63**, 224204 (2001).
- [95] P. W. Brouwer, M. Duckheim, A. Romito, and F. von Oppen, Probability distribution of Majorana end-state energies in disordered wires, *Phys. Rev. Lett.* **107**, 196804 (2011).
- [96] A. A. Clerk, M. H. Devoret, S. M. Girvin, F. Marquardt, and R. J. Schoelkopf, Introduction to quantum noise, measurement, and amplification, *Rev. Mod. Phys.* **82**, 1155 (2010).
- [97] F. Nathan and M. S. Rudner, Universal Lindblad equation for open quantum systems, *Phys. Rev. B* **102**, 115109 (2020), [arXiv:2004.01469](https://arxiv.org/abs/2004.01469).
- [98] Microsoft Quantum, Simulating the RF response of mesoscopic devices, to be published (2024).
- [99] R. V. Mishmash, B. Bauer, F. von Oppen, and J. Alicea, Dephasing and leakage dynamics of noisy Majorana-based qubits: Topological versus Andreev, *Phys. Rev. B* **101**, 075404 (2020).
- [100] P. Pakkiam, A. V. Timofeev, M. G. House, M. R. Hogg, T. Kobayashi, M. Koch, S. Rogge, and M. Y. Simmons, Single-shot single-gate rf spin readout in silicon, *Phys. Rev. X* **8**, 041032 (2018).
- [101] A. West, B. Hensen, A. Jouan, T. Tanttu, C.-H. Yang, A. Rossi, M. F. Gonzalez-Zalba, F. Hudson, A. Morello, D. J. Reilly, and A. S. Dzurak, Gate-based single-shot readout of spins in silicon, *Nat. Nanotechnol.* **14**, 437–441 (2019).
- [102] M. Urdampilleta, D. J. Niegemann, E. Chanrion, B. Jadot, C. Spence, P.-A. Mortemousque, C. Bäuerle, L. Hutin, B. Bertrand, S. Barraud, R. Maurand, M. Sanquer, X. Jehl, S. D. Franceschi, M. Vinet, and T. Meunier, Gate-based high fidelity spin read-out in a CMOS device (2018), [arXiv:1809.04584](https://arxiv.org/abs/1809.04584).